

A *Chandra* Study of the Rosette Star-Forming Complex. III. The NGC 2237 Cluster and the Region's Star Formation History

Junfeng Wang,^{1,2} Eric D. Feigelson,¹ Leisa K. Townsley,¹ Patrick S. Broos,¹ Carlos G. Román-Zúñiga,³ Elizabeth Lada,⁴ and Gordon Garmire¹

ABSTRACT

We present high spatial resolution *Chandra* X-ray images of the NGC 2237 young stellar cluster on the periphery of the Rosette Nebula. We detect 168 X-ray sources, 80% of which have stellar counterparts in USNO, 2MASS, and deep FLAMINGOS images. These constitute the first census of the cluster members with $0.2 \lesssim M \lesssim 2 M_{\odot}$. Star locations in near-infrared color-magnitude diagrams indicate a cluster age around 2 Myr with a visual extinction of $1 \lesssim A_V \lesssim 3$ at 1.4 kpc, the distance of the Rosette Nebula's main cluster NGC 2244. We derive the K-band luminosity function and the X-ray luminosity function of the cluster, which indicate a population ~ 400 –600 stars. The X-ray-selected sample shows a *K*-excess disk frequency of 13%. The young Class II counterparts are aligned in an arc ~ 3 pc long suggestive of a triggered formation process induced by the O stars in NGC 2244. The diskless Class III sources are more dispersed. Several X-ray emitting stars are located inside the molecular cloud and around gaseous pillars projecting from the cloud. These stars, together with a previously unreported optical outflow originating inside the cloud, indicate that star formation is continuing at a low level and the cluster is still growing.

This X-ray view of young stars on the western side of the Rosette Nebula complements our earlier studies of the central cluster NGC 2244 and the embedded clusters on the eastern side of the Nebula. The large scale distribution of the clusters and molecular material is consistent with a scenario in which the

¹Department of Astronomy & Astrophysics, The Pennsylvania State University, 525 Davey Lab, University Park, PA 16802

²Current Address: Harvard-Smithsonian Center for Astrophysics, 60 Garden Street, Cambridge, MA 02138; juwang@cfa.harvard.edu

³Centro Astronómico Hispano Alemán, Camino Bajo Huétor 50, Granada, Spain 18008

⁴Department of Astronomy, University of Florida, 211 Bryant Space Science Center, Gainesville, FL 32611

rich central NGC 2244 cluster formed first, and its expanding HII region triggered the formation of the now-unobscured satellite clusters RMC XA and NGC 2237. A large swept-up shell material around the HII region is now in a second phase of collect-and-collapse fragmentation, leading to the recent formation of subclusters. Other clusters deeper in the molecular cloud appear unaffected by the Rosette Nebula expansion.

Subject headings: Open clusters and associations: individual (NGC 2237, NGC 2244) - ISM: individual (Rosette Nebula) - stars: formation - stars: pre-main sequence - X-Rays: stars

1. Introduction

The triggered formation of the lower mass stars in the vicinity of massive stars is a complex process that is only now being characterized in detail (see Briceño et al. 2007, for a recent review). In their immediate neighborhood, massive stars suppress further star formation by quickly ionizing and dispersing surrounding molecular material (Herbig 1962). At greater distances, OB stars are more constructive to star formation activity; the shocks driven by ionization or stellar winds are crucial in triggering the collapse of molecular cores (Whitworth et al. 1994; Lefloch & Lazareff 1994). Triggered star formation events by massive stars have been observed at different spatial scales, for example, small bright-rimmed clouds on the periphery of HII regions (Sugitani et al. 1995; Getman et al. 2007; Ogura et al. 2007), an embedded cluster in a molecular cloud core on the edge of the dispersed Cep OB3b (Getman et al. 2006), multiple generations of star formation in W5 (Koenig et al. 2008), a broad ridge of young stars along the southwestern boundary of M 17 (Jiang et al. 2002; Broos et al. 2007), and a rich secondary cluster on the edge of Sharpless 219 (Deharveng et al. 2006).

The Rosette star forming complex has been considered an excellent candidate for triggered star formation (Cox et al. 1990; Phelps & Lada 1997) following the framework developed by Elmegreen & Lada (1977). The massive young cluster NGC 2244 ($d \sim 1.4$ kpc, $t \sim 2$ Myr; Hensberge et al. 2000) powers a visually spectacular expanding HII region known as the Rosette Nebula. The ionized nebula is clearly interacting with the adjacent Rosette Molecular Cloud (RMC) to the east of the Nebula which has a collection of embedded young stellar clusters, each with a few hundred pre-main sequence stars (Table 6 in Wang et al. 2009; see also Poulton et al. 2008). However, recent investigations of the ages and disk fractions of these embedded stellar populations at near-infrared (NIR), mid-infrared, and X-ray wavelengths do not obviously support a sequential, triggered origin (Román-Zúñiga et al. 2008a;

Poulton et al. 2008; Wang et al. 2008). Instead, Wang et al. suggest that the previously unnoticed, more evolved, and less-obscured RMC XA cluster lying between NGC 2244 and the molecular cloud may have been triggered by the expanding Rosette HII region ~ 2 Myr in the past.

To the west of NGC 2244 cluster lies the NGC 2237 cluster¹. NGC 2237 was not studied until the recent 2MASS and FLAMINGOS *JHK* surveys (Li 2005; Román-Zúñiga et al. 2008a; Bonatto & Bica 2009). Li (2005) estimates that the cluster has a diameter of 3.2 pc with a population of 232 stars. Bonatto & Bica (2009) studied NGC 2237 (called NGC 2239) with field-star-decontaminated 2MASS photometry, and suggested that it may be a young (5 ± 4 Myr) cluster located in the background of NGC 2244 ($d = 3.9$ kpc). In the Digital Sky Survey optical plate (Figure 1), the NGC 2237 region lies on the boundary between the HII region and the cold neutral molecular material (Core E; Blitz & Thaddeus 1980; Román-Zúñiga & Lada 2008b) on the western side of the nebula. Numerous dusty elephant trunks and pillars point towards the O stars in NGC 2244. Its structure contributes to the petal-like morphology of the Rosette Nebula and resembles the pillared boundaries of other HII regions such as M 16 and IC 1396 where the molecular cloud is photoionized and ablated by the O star ultraviolet light and winds.

However, the stellar content of NGC 2237 has not been well-characterized and most of its members have not been individually identified. The difficulty is that the near-infrared surveys are dominated by older field stars unrelated to the Rosette star forming complex so that only the statistical enhancement in stellar surface density, and the fraction of members with *K*-band excesses, have been studied. X-ray surveys are more effective at uncovering the full pre-main sequence (PMS) population of young clusters. Low mass young stars emit X-rays from violent magnetic reconnection flares, orders of magnitude more luminous than seen in older Galactic stars (see review by Feigelson et al. 2007). Hence, an X-ray study can individually identify young stars including the diskless Class III sources missed in the infrared-excess samples. X-ray studies of NGC 2244 (Wang et al. 2008, henceforth Paper I) and the embedded clusters in the RMC (Wang et al. 2009, Paper II) on the eastern

¹The designations of clusters and nebulae in the Rosette region have been confused since the 19th century. NGC 2237 refers both to the stellar cluster and its associated nebulosity on the west side of the Rosette nebula (Sulentic & Tifft 1973). The star cluster is listed as Ocl 512 in the catalogue of Alter et al. (1970) and included in the study of the Monoceros star clusters by Pérez (1991). NGC 2238 and 2246 are old designations for bright emission regions around the Rosette Nebula; these names are rarely used today. The well-studied rich star cluster exciting the nebula is NGC 2244; NGC 2239 is an obsolete designation for this central cluster. The listing in the SIMBAD database for NGC 2237 was incorrect until recently. Note that the open cluster NGC 2239 studied in Bonatto & Bica (2009) in fact refers to NGC 2237. A thorough review of the Rosette star formation complex is provided by Román-Zúñiga & Lada (2008b).

side of the Rosette Nebula produced a richer census of young stars than available from infrared-excess studies. A handful of X-ray stars in NGC 2237 have been identified with the *ROSAT* satellite (see Berghöfer & Christian 2002), but observations with the *Chandra X-ray Observatory* with its high spatial resolution and sensitivity, are much more effective.

In this paper (the third in a series on the Rosette Complex), we focus on the X-ray point sources identified in the image of the NGC 2237 region obtained with the *Chandra X-ray Observatory*. We identify over 150 individual X-ray emitting young stars and investigate their spatial distribution and stellar properties to study the star formation activity on the western side of the Rosette Nebula. Proximity to dense molecular structures and correlated age-spatial gradients in the stellar distributions are particularly valuable in evaluating the timescale and efficiency of the triggering process that may have occurred. We combine these results on NGC 2237 with earlier work on the central NGC 2244 cluster and the embedded RMC clusters to elucidate a large-scale view of the star formation history in the Rosette complex. A distance of $d = 1.4$ kpc to NGC 2237 is adopted throughout the paper and the uncertainty in distance (see Bonatto & Bica 2009) will be discussed.

2. Chandra Observations and Data Reduction

The NGC 2237 region was observed with the Imaging Array of the *Chandra* Advanced CCD Imaging Spectrometer (ACIS-I) which has a field of view $\sim 17' \times 17'$. The 20 ks ACIS-I observation was conducted on 9 February 2007, in the “Timed Event, Very Faint” mode with $5 \text{ pixel} \times 5 \text{ pixel}$ event islands (see Table 1 in Paper I for details of pointing and roll angle). The pointings towards NGC 2237 and NGC 2244 are outlined in Figure 1.

We follow the data reduction and source extraction procedures described in Paper I. The ACIS-I image is shown in Figure 2. A smoothed, exposure corrected X-ray image is created with the CIAO tool *csmooth* (Ebeling et al. 2006) and shown in Figure 3, which gives the relative spectral hardness of the sources. 65% of the sources are dominated by soft band (0.5-2.0 keV) X-ray emission with median photon energy < 2 keV, implying relatively low obscuration. A candidate source list was obtained using the *wavdetect* program (Freeman et al. 2002), supplemented a few possible sources found by visual inspection. Events are extracted and analyzed for each candidate source using our IDL script *ACIS Extract*² (version 3.128; hereafter *AE*, Broos et al. 2010). After a careful review of the net counts distribution for all candidate sources, we rejected sources with greater than 1% likelihood of arising from a background fluctuation assuming Poisson statistics ($P_B > 0.01$). Only the brightest source

²http://www.astro.psu.edu/xray/docs/TARA/ae_users_guide.html

in the field (#149) has more than 100 source counts.

The trimmed source list includes 168 valid X-ray detections, which are further divided into a primary list of 130 highly reliable sources (Table 1) and a secondary list of 38 tentative sources with $0.001 \leq P_B < 0.01$ likelihood of being spurious background fluctuations. The resulting sources and X-ray properties are reported in Table 1 and 2 which are very similar to the source tables in Townsley et al. (2006), Broos et al. (2007), and Paper I. Descriptions of the table columns are given in the table footnotes. Six sources (#160, 163, 164, 166, 167, and 168) are in the ACIS region overlapping the NGC 2244 field described in Paper I. Four of these (#163, 166, 167, and 168) were detected in the earlier ACIS exposure. One bright source (#149) was found in the *ROSAT* study of Berghöfer & Christian (2002).

Source event arrival times were compared to that of a uniform light curve model in *AE*, and five sources (#4, 39, 118, 149, and 152) were found to be significantly variable ($P_{KS} < 0.005$ in column 15 of Tables 1 and 2) during the short 20 ks observation. The light curve of #149 shows a typical X-ray flare seen in PMS stars (e.g. Wolk et al. 2005) captured in the rise phase near the end of the observation.

For the 65 sources with photometric significance $Signif > 2.0$ (column 12 in Tables 1 and 2), the extracted spectra were fit with a single temperature *apec* thermal plasma model (Smith et al. 2001) subjected to an absorbing column of interstellar material (Wilms et al. 2000, *tbabs* model;) with the *XSPEC*³ package (version 12.2.1ap, Arnaud 1996). The best-fit model was obtained with the maximum likelihood method (Cash 1979). Abundances of $0.3 Z_{\odot}$ were assumed for the automated fitting performed by *AE*. Spectral results are presented in Table 3; table notes describe the columns and unusual cases. Absorbing column densities range from negligible to $\log N_H \sim 23.2 \text{ cm}^{-2}$, equivalent to a visual absorption of $A_V \sim 100 \text{ mag}$ (Vuong et al. 2003). Temperatures range from $kT \sim 0.1 \text{ keV}$ to $kT > 15 \text{ keV}$; this truncated value reflects the hardest spectra detectable by the ACIS detector. The range of total band (0.5 – 8 keV) absorption-corrected luminosities derived from spectral modeling is $30.0 \lesssim \log L_{t,c} \lesssim 32.1 \text{ ergs s}^{-1}$.

To estimate the X-ray sensitivity of the ACIS exposure, we use the Portable, Interactive Multi-Mission Simulator (PIMMS) software⁴ for a limiting on-axis source with 3 counts assuming a 2 keV plasma temperature and an absorbing column $\log N_H \sim 21.4 \text{ cm}^{-2}$ (corresponding to $A_V = 1.5 \text{ mag}$ visual extinction). The resulting limiting total band luminosity as observed by the telescope is $\log L_t \sim 29.4 \text{ ergs s}^{-1}$ and limiting intrinsic luminosity

³ <http://heasarc.gsfc.nasa.gov/docs/software/lheasoft/xanadu/xspec>

⁴ <http://heasarc.gsfc.nasa.gov/docs/software/tools/pimms.html>

$\log L_{t,c} \sim 29.6$ ergs s⁻¹. A conservative estimate for limiting luminosity of the entire NGC 2237 observation, including sensitivity degradation due to off-axis optics and higher absorption, is $\log L_t \sim 30.0$ erg s⁻¹. Using the empirical correlation between X-ray luminosity and mass in PMS stars from well-studied samples in the Orion and Taurus clouds (Preibisch et al. 2005; Telleschi et al. 2007), we infer that the observation is complete to all cluster members down to $M \sim 1.0 M_\odot$ and includes an incomplete fraction of cluster members down to $M \sim 0.2 M_\odot$.

3. Stellar Counterparts to *Chandra* Sources

3.1. Correlation of X-ray and Optical/Infrared Catalogs

We searched optical and infrared catalogs from the literature and recent observations for stellar counterparts to these 168 X-ray sources. In addition to the available catalogs listed in Paper II (USNO, 2MASS, and FLAMINGOS), other catalogs are: *UBV* photometry of NGC 2244 (Ogura & Ishida 1981, OI81; Massey et al. 1995, MJD95), *BVIRH_α* photometry of NGC 2244 (Berghöfer & Christian 2002, BC02). *Spitzer Space Telescope* mid-infrared observations are not yet available for this field. The reference frame offsets between the ACIS field (which is astrometrically aligned to the Hipparcos frame using 2MASS sources in the data reduction) and the catalogs are 0.3'' to OI81, 0.4'' to MJD95, 0.3'' to BC02, 0.2'' to USNO, and 0.2'' to FLAMINGOS. These offsets were applied before matching sources.

We associate ACIS X-ray sources with optical and near IR (ONIR) sources using positional coincidence based on the positional uncertainties of the X-ray sources and stellar catalogs (Broos et al. 2007). Likely associations for 134 of the 168 ACIS sources are given in Table 4 along with ONIR photometric data (see Table 4 footnote for photometric errors). Typical offsets between the X-ray and near-infrared sources are 0.2'' for on-axis sources and 0.7'' for off-axis sources. Although USNO photometry is reported when optical counterparts are found, readers are cautioned that magnitudes are derived from photographic plates with ~ 0.3 magnitude photometric accuracy (Monet et al. 2003). *JHK* magnitudes from 2MASS are given when the source falls outside the FLAMINGOS field of view. The SIMBAD and VizieR online catalogs are searched for complementary information with results given in the table footnotes.

The *Chandra* observation is able to identify a majority of the estimated ~ 230 members of the NGC 2237 cluster (Li 2005). This excellent result arises from a combination of three effects: the short ACIS exposure is sufficient to detect a large fraction of the stellar initial mass function (IMF), even with significant obscuration (§2); the catalog from FLAMINGOS

deep JHK imaging is sensitive to most of the cluster population; and the X-ray image suffers only minor contamination from non-cluster X-ray sources (§ 3.3).

3.2. Near-infrared and Disk Properties

The $J - H$ vs. $H - K$ color-color diagram for 119 *Chandra* stars is shown in Figure 4. This sample is restricted to stars with high-quality JHK photometry (i.e., errors in both $J - H$ and $H - K$ colors < 0.1 mag). Most *Chandra* sources occupy the color space associated with diskless young stars, Class III or weak-lined T Tauri stars (WTTS), that are reddened by interstellar extinction. A concentration of cluster members subjected to $A_V \sim 2$ mag is apparent, approximately centered at $J - H = 0.80$ and $H - K = 0.35$. This is also the typical extinction seen towards NGC 2244 (e.g., Ogura & Ishida 1981; Berghöfer & Christian 2002). Seven stars with K -band excesses lie to the right of this reddening band⁵, defined as stars that have colors $(J - H) > 1.7(H - K) + 2\sigma(H - K)$. These are likely PMS stars with circumstellar accretion disks, Class II objects or classical T Tauri stars (CTTS). One outlier among the Class III sources, #86, appears highly obscured with $A_V \sim 20$ mag. Among the faintest X-ray sources with only 4 net counts in the ACIS image, this source is located in an optically dark region; this source is discussed in § 4.2. We did not detect the red sources in Román-Zúñiga et al. (2008a) with no detection in J and $H - K > 1.5$ mag, the majority of which were located within the molecular cloud (cf. Figure 27 in Román-Zúñiga et al.). However, four ACIS sources (#45, 70, 73, 85) have only K -band counterparts with no J and H detections, and hard median photon energy (~ 2.5 keV). They are probably deeply embedded young stars, similar to those red sources.

Figure 5 shows the NIR J vs. $J - H$ color-magnitude diagram (CMD) for the same stars presented in Figure 4. The 1 Myr and 2 Myr PMS isochrones from the evolutionary tracks of Siess et al. (2000) are shown for reference. If the NGC 2237 satellite cluster was triggered by the central NGC 2244 cluster, it must be younger than NGC 2244 at ~ 2 Myr (Hensberge et al. 2000). While it is not possible to directly measure the age of NGC 2237 without obtaining spectra of the cluster members, the distribution of stars in NGC 2237 in the NIR color-magnitude diagram is nearly identical to that seen in the main NGC 2244 cluster (cf. Figure 6 of Paper I). Approximate stellar masses can be measured from the iso-mass vectors (blue dashed lines) on the color-magnitude diagram. They range from early-B

⁵These sources are #44, 61, 80, 97, 111, 117, and 121. For the two sources (#111 and #121) that are close to the reddening band, the errors in both $J - H$ and $H - K$ colors are small, ~ 0.015 mag, therefore their K -excesses are small but statistically significant. See also Paper I for a brief discussion on systematics in the K -excess. These stars are also present in Román-Zúñiga et al. (2008a).

stars to early-M stars.

From Figures 4 and 5, we find that the fraction of K-band excess sources is 13% among stars with $M \gtrsim 1 M_{\odot}$, where we estimate masses from the NIR color-magnitude diagram (recall this is also the completeness limit of the X-ray-selected stars). This closely matches the K -excess disk fraction of $15 \pm 3\%$ reported in the FLAMINGOS NIR study of NGC 2237 (Román-Zúñiga et al. 2008a). However, when the full X-ray sample including many sub-solar mass stars is considered, the K -band excess fraction of the X-ray sample is 6%. Since disks around intermediate-mass stars evolve faster than disks around low-mass stars (e.g., Hernández et al. 2007), most likely this is a selection effect against the X-ray emission from CTTS which are known to be systematically lower than the X-rays from WTTS by a factor of 2 (e.g., Preibisch et al. 2005).

3.3. Non-cluster Contaminants and Embedded Sources

We deduce from previous studies (e.g., Wang et al. 2007) that the 34 ACIS sources without any matched counterparts are a mixture of newly discovered embedded cluster members, distant background stars, and extragalactic sources. The level of contamination by extragalactic X-ray sources and Galactic disk stars is evaluated with simulations as described in Paper I. The extragalactic population is simulated by placing artificial sources randomly across the detector with incident fluxes drawn from the X-ray background $\log N$ – $\log S$ distribution (Moretti et al. 2003). The Galactic stellar population expected in the direction of our ACIS field is simulated with the stellar population synthesis model of Robin et al. (2003), adopting X-ray luminosity distributions of nearby stars measured from *ROSAT* surveys (e.g., Hünsch et al. 1999). These simulations predict that ~ 12 sources will be extragalactic and ~ 10 could be old field stars. These contaminants constitute $\sim 13\%$ of the 168 ACIS sources. Figure 7 compares the spatial distribution of X-ray sources without NIR counterparts and sources that have hard median photon energies ($E_{med} > 2.0$ keV). The 10 unidentified X-ray sources that are located in the unobscured HII region cavity should have counterparts if they are cluster members. These sources, plus a few in the obscured region, are most likely the background extragalactic sources and background field stars. The other 24 ACIS sources lie in the molecular pillars and the optically darker regions with dense molecular material. They are likely new embedded low-mass PMS stars that are fainter than the FLAMINGOS completeness limit. Such X-ray-discovered stars are commonly found in the molecular clouds surrounding other clusters (Getman et al. 2005a; Broos et al. 2007, Paper I).

3.4. Properties of Selected Stars

A few stars have bright J magnitudes indicating they are intermediate-mass stars (B and A types) reddened from the ZAMS with $0 < A_V < 2$ mag. Their locations in the color-color diagram (Figure 4) are also consistent with early spectral types, and their bright optical counterparts are identified by OI81, MJD95 or other studies. Two of these sources (#44 and #61) have masses $M > 2M_\odot$ estimated from the color-magnitude diagram and strong K -band excesses; these are good candidates for being accreting Herbig Ae/Be (HAeBe) stars. Others do not show NIR excess. Wang et al. (2007) also find that in massive OB cluster NGC 6357, over 90% of the X-ray selected intermediate-mass stars are not HAeBe stars. Perhaps this is related to the fast disk evolution in the HAeBe stars (e.g., Waters & Waelkens 1998), or an X-ray deficiency in detecting the intermediate stars with NIR-excess disks (e.g., Hamaguchi et al. 2005).

ACIS source #53 is a B1 star (Philip & Egret 1980), the earliest spectral type known in the NGC 2237 region. It only has 16 net counts and the spectral fitting gives $\log L_{t,c} \sim 30.2$ erg s $^{-1}$. A B2 star identified by Philip & Egret (1980) is source #54 in our X-ray study. With over 100 counts, its X-ray spectrum can be reasonably well-determined (Table 3 and Figure 6a): it is dominated by a plasma with moderate temperature ($kT = 1.2$ keV) with low absorption ($\log N_H \sim 20.0$ cm $^{-2}$) and X-ray luminosity $\log L_{t,c} \sim 31.0$ erg s $^{-1}$ (0.5–8 keV). These X-ray properties are similar to those of other early-B stars; for example, in the Orion Nebula Cluster (Stelzer et al. 2005, ONC;) and NGC 2244 Rosette Cluster (Paper I).

Source #149 is the X-ray source with most net counts in this study with a spectrum well-fit by a single plasma of $kT = 4.1$ keV and absorption column of $\log N_H \sim 21.3$ cm $^{-2}$ (Figure 6b). The kT value is higher than that of a typical PMS star (e.g., Güdel et al. 2007), caused by the X-ray flare seen near the end of the observation. It is known from previous observations that spectral hardening is commonly seen during X-ray flaring in PMS stars (e.g., Getman et al. 2008a). The absorption corrected total band (0.5–8 keV) X-ray luminosity $\log L_{t,c} \sim 31.3$ erg s $^{-1}$. Berghöfer & Christian (2002) reported a similar level of $\log L_x = 31.01$ erg s $^{-1}$ (0.5–2 keV) in their *ROSAT*/PSPC observation. This source represents one of the typical flaring PMS stars seen in the ONC (Wolk et al. 2005; Getman et al. 2008a) and many other young star clusters (Wolk et al. 2008).

Lastly, ACIS source #20 is very interesting in its X-ray properties, showing a high X-ray luminosity ($\log L_{t,c} \sim 31.3$ erg s $^{-1}$), hard spectrum ($kT \sim 3.4$ keV), and high absorption ($N_H \sim 10^{23}$ cm $^{-2}$). It is located in the optically dark pillar region at the peripheries of the HII nebula. No counterpart is found in the 2MASS image and the FLAMINGOS image, and no information on its mid-IR or mm band properties is currently available. It may represent a similar detection of Class 0/I protostar as the VLA/BIMA source IRAS 21391+5802 in IC

1396N (Getman et al. 2007) or a chance superposition of a background AGN.

4. Cluster Properties

4.1. Cluster Center

The central position of the NGC 2237 cluster has not been well-determined from NIR observations. Li (2005) obtains $(\alpha, \delta) = (6^h30^m55.8^s, +04^\circ58'30'')$ from a weak 2MASS surface density enhancement, while Román-Zúñiga et al. (2008a) obtains $(6^h30^m22^s, +04^\circ56')$ from the *K*-band excess sources in the deeper FLAMINGOS data (see Table 1 in Román-Zúñiga et al. 2008a). The 2MASS position is $\sim 8'$ east of the FLAMINGOS position.

The X-ray position for the cluster core and the spatial distributions of stellar populations are best examined from a smoothed map of the X-ray selected cluster members. Following our Papers I and II, we derived a smoothed map of the surface density of the X-ray-selected cluster members using a $1.5'$ -radius top-hat smoothing kernel (Figure 8). To reduce the effect of sensitivity variations across the field, we included only 93 sources that have 6 or more net counts. Adopting different kernel widths does not have a significant effect on the resulting features discussed here. The stellar density in the western portion of the field with molecular cloud material is likely underestimated compared to the eastern portion for two reasons: 24 unidentified X-ray sources are probably embedded stars (§ 3.3) and the sensitivity to embedded stars is reduced due to soft X-ray absorption.

A clear peak stellar concentration appears at $(6^h31^m00^s, +04^\circ58')$. This is the most accurate available as the X-ray contour map has a much higher dynamic range due to its smaller contamination by extraneous sources. This position derived from the *Chandra* selected stars is consistent with the low-resolution *ROSAT* X-ray image shown by Berghöfer & Christian (2002), and agrees reasonably well with 2MASS result, lying $1'$ towards the main NGC 2244 cluster. The discrepancy in the infrared cluster centroids is due to different fields of view, definition of cluster center, and possibly age effects: the FLAMINGOS field extends $\sim 10'$ westward of the ACIS field, and Román-Zúñiga et al. (2008a) choose to define the cluster to encompass Class II systems found in this extended region, while the X-ray map and the 2MASS *K* surface density are weighted toward Class III sources. Our X-ray star distribution shows a secondary peak $8'$ northwest of the primary peak (see § 4.2), which is close to the NGC 2237 core position defined in Román-Zúñiga et al. (2008a).

4.2. Spatial Distribution of the Young Stars

The spatial distribution of cluster members has not been well-established from NIR studies due to the high contamination level of non-cluster stars. The diameter of the NGC 2237 cluster has been estimated to be ~ 3.2 pc ($8'$) from the 2MASS enhancement (Li 2005) and 3.8 pc from the K -band excess stars (Román-Zúñiga et al. 2008a). Our X-ray-selected NGC 2237 stars, which represent the bulk of cluster members, indicate that the structure is more complex than a spherical aggregate with a single size.

From Figure 8, we see that the dimension of the main stellar concentration around the cluster core at ($6^h31^m00^s$, $+04^\circ58'$) is $\sim 6' \times 3'$ ($\sim 2.5 \times 1.3$ pc) in diameter, asymmetrically elongated towards the west from the dense core. A sparse secondary stellar concentration may also be present: a northwestern group of ~ 15 stars in a 1.5×1 pc region around ($6^h30^m39^s$, $+05^\circ00'$).

We next investigate whether any spatial segregation is seen in stars at different stages of PMS evolution. Figure 9 shows the distribution of X-ray-selected Class II and Class III sources classified using the near-infrared color-color diagram (Figure 4). The 34 sources without matched counterparts, many of which are probably embedded stars (§ 3.3), are also shown. The seven Class II sources appear to be aligned along an arc parallel to the edge of the dusty cloud edge and perpendicular to the direction towards the early O stars in NGC 2244. Most of the Class III sources are associated with the groupings mentioned above; the southern and eastern edges of the field seem to lack X-ray sources. The CO emission contours suggest that there is some molecular material to the west. The sensitivity of our observation is too shallow to probe the star formation activity here because of heavy absorption.

Figure 10 shows the spatial distribution of stars in different mass ranges. We consider stars with identified B and A spectral types (see Table 4 footnote) and stars with NIR-estimated masses $\gtrsim 2M_\odot$ as the high mass sample, while stars in the mass range $M < 2M_\odot$ are the low mass sample. The high mass stars are spatially concentrated at the cluster center. Note that sources #44, 53, and 61 lie along the same arc as the K -band excess Class II sources. In contrast, the majority of the low mass stars are not strongly clustered, but are dispersed along the peripheries of the HII region and inside the dark cloud. Again, the deficit of sources in the southern and western edges of the field is worth noting.

A close-up $H\alpha$ image (Li & Rector 2004) of a small region at the interface between the HII region and the cloud is shown in Figure 11. A number of X-ray stars are found at or near the tip of dusty pillars (ACIS #77, 86, 91, 96, 100, and 101) in the two regions outlined by circles. The *Chandra* images of the Eagle Nebula (M 16) and NGC 6357 are similar with a handful of hard-spectrum X-ray stars embedded in dusty pillars on the edges of HII regions

ionized by rich clusters (Linsky et al. 2007, Wang et al. 2007). It is plausible that these stars become exposed because the OB stars of NGC 2244 (to the east) have photoevaporated the surrounding cloud material. The most obscured source, #86, is embedded in or behind the southern pillar shown. Only 4 counts are seen from this source, most above 2 keV. Li (2005) also noted a highly obscured 2MASS source with extinction $A_V \sim 17$ mag located behind the same pillar object, however no matching X-ray source was detected in our observation, likely due to the limited sensitivity.

Another interesting feature in this region is a bright visually identified outflow outlined by the white box in Figure 11. Located at ($6^h30^m48.7^s$, $+05^\circ01'44''$), it has not been reported previously in the literature, to our knowledge. This may be a Herbig-Haro (HH) object. There is a visible star $30''$ to the northwest aligned with the outflow which might be its host star. No X-rays are detected from the candidate ionizing star or from the jet.

We thus find that the spatial distribution of the *Chandra* stars (Figure 8) and their NIR counterparts (Figure 9) show the following features: a compact cluster previously recognized as NGC 2237 which is $\sim 2.5 \times 1.3$ pc in size, elongated along an east-west axis parallel to the direction of the NGC 2244 early O stars. Its shape might reflect an origin in a cometary cloud that was triggered to form stars and ablated by the O star ultraviolet photons and winds. A broader distribution of stars with a possible sparse subcluster is seen over a 5×5 pc region northwest of the main cluster, partly in the evacuated Rosette HII region and partly embedded in the optically dark pillars and cloud. The young star density is distinctly reduced 1–3 pc south and west of the cluster; the western deficit can be attributed to absorption from the residual molecular cloud material. This NGC 2244 satellite cluster contains about ten intermediate-mass stars, consistent with its estimated population from the 2MASS study. There are hints of mass segregation (the intermediate mass stars lie primarily in the HII region) and age segregation (the *K*-band excess stars lie primarily along the cloud edge), but a clear age sequence is not seen. We note that richer substructures in the stellar distributions of massive young clusters have been seen in our X-ray studies of NGC 6357 (Wang et al. 2007), M 17 (Broos et al. 2007), NGC 2244 (Paper I), and NGC 6334 (Feigelson et al. 2009).

4.3. K-band and X-ray Luminosity Functions

Following Li (2005) and Wang et al. (2008) we create the apparent K_s -band luminosity function (KLF) for NGC 2237 with the spatially complete 2MASS data, subtracting the KLF of a control field representative of the background distribution of NGC 2237 and reddened with $A_V = 2$ mag. Our KLF, shown in Figure 12, is consistent with the one derived for NGC 2237 in Bonatto & Bica (2009), which turns over beyond the completeness limit of 2MASS

($K_s = 14.3$ mag; Skrutskie et al. 2006). It is well fit with a power-law distribution in the range $12 < K_s < 14.3$ mag, giving a slope of ~ 0.6 . Within uncertainties, this is marginally consistent with model predictions of ~ 0.4 for clusters of similar ages (Lada & Lada 1995). A significant excess of stars is seen as a “bump” at $K_s = 11.5$ in the KLF (see also Figure 12 in Bonatto & Bica 2009), indicating the presence of more intermediate-mass stars than expected from a simple extension of the KLF slope. This perhaps reflects the contribution from a secondary cluster in the field or foreground/background stars. For comparison, the KLF for the young, embedded cluster RMC XC (Paper II) is also derived and shown in Figure 12. No excess of K -bright stars is seen in the KLF and the slope is 0.39, in agreement with the KLF slopes in Lada & Lada (1995).

We further examined the 13 K -bright stars to identify their nature. The contamination of bright stars from NGC 2244, the central cluster in the Rosette Nebula, is too small to account for the K -bright stars found. Radial profiles of NGC 2244 (Figure 2 in Li 2005; see also Paper I) show that the stellar surface density of NGC 2244 is approximately 0.2 star per square arcmin at a distance $r \sim 15'$ from the cluster center and has already decreased to zero at $r \sim 19'$. At most two NGC 2244 stars may be present in the NGC 2237 region, which would not necessarily be K -bright stars even if they are detected.

Three of these K -bright stars are not detected as X-ray sources, so they are most likely nearby foreground stars along the line of sight towards NGC 2237. For the remaining 10 X-ray-detected K -band bright sources⁶, their median photon energy ranges between 1 and 1.5 keV. None shows very soft emission (median energy $\ll 1$ keV) that is suggestive of foreground stars with low absorption. Using B and V magnitudes from the NOMAD catalog (Zacharias et al. 2005), we derived the optical CMD for these stars, shown in Figure 13. Adopting the tabulated spectral types and photometric properties of stars in Schmidt-Kaler (1982), the zero-age main sequence (ZAMS) isochrone is shown, assuming a minimum reddening of $E(B - V) = 0.5$ and a distance of $d = 1.4$ kpc for NGC 2237 members. Four stars (#54, 59, 83, 138) appear to be likely foreground FGK stars; the ZAMS location at $d = 1$ kpc with no reddening is shown for reference. The rest are consistent with being intermediate-mass stars in NGC 2237.

Similarly we derived the observed hard band XLF (see Wang et al. 2008) for NGC 2237, which is more robust against the inhomogeneous obscuration. Luminosities were taken from the spectral fits for the brighter X-ray sources, and estimated with a simple absorbed thermal plasma model for the faintest sources with few counts. We adopt an $N_H = 4 \times 10^{21} \text{ cm}^{-2}$ (derived from $N_H/A_V = 1.6 \times 10^{21} \text{ cm}^{-2} \text{ mag}^{-1}$; Vuong et al. 2003, and a typical measured

⁶These sources are ACIS# 44, 53, 54, 59, 71, 83, 128, 129, 138, and 141.

$A_V \sim 2.5$ mag from Figure 4), and a $kT = 2$ keV based on the median photon energy of the faint sources (Feigelson et al. 2005). The XLF with a farther distance $d = 3.9$ kpc was also generated similarly, except that a higher $N_H = 5.5 \times 10^{21} \text{ cm}^{-2}$ is adopted (Bonatto & Bica 2009).

Figure 14 shows the resulting XLF. The uncertainties for the hard band luminosity L_h derived from spectral fits range between 0.1 and 0.3 dex. To include both the \sqrt{N} counting error and the Lx -dependent measurement error, following Getman et al. (2006), XLF error bars shown in Figure 14 cover the range containing 68% (1σ equivalent) of the Monte Carlo simulated XLF distributions, where individual X-ray luminosities are randomly drawn from Gaussian distributions with mean equal to the measured $\log L_h$ and variances ~ 0.3 dex (observed $\Delta \log L_h$).

For comparison, the XLF for NGC 2244 and the XLF for ONC from the Chandra Orion Ultradeep Project (COUP Getman et al. 2005b) were included. Considering $\log L_h \gtrsim 29.6$ erg s $^{-1}$, where the detections are mostly complete, the slope of the NGC 2237 XLF matches the ONC XLF well, but a scaling factor ~ 0.2 – 0.3 is required to fit the ONC X-ray-detected population. Given that the ONC contains ~ 2000 members with mass above the stellar limit (e.g., Hillenbrand 1997), this implies a smaller cluster population ~ 400 – 600 for NGC 2237. The X-ray-inferred population agrees well with the NIR population of ~ 230 stars above $0.8 M_\odot$, which is $\sim 40\%$ of the total population assuming a standard IMF. In addition, comparison of the NGC 2237 KLF to the RMC XC cluster KLF (Figure 12) also supports that NGC 2237 is less rich than the RMC XC cluster, which has an estimated population of ~ 800 stars (Paper II). We conclude that NGC 2237 contains ~ 400 – 600 members.

4.4. Discussion on the Distance to NGC 2237

The adopted distance to NGC 2237 in this work is $d \sim 1.4$ kpc, consistent with the generally accepted distance to the Rosette region (e.g., Ogura & Ishida 1981; Román-Zúñiga & Lada 2008b). A spectroscopic survey is needed to securely establish the distance to NGC 2237. In Bonatto & Bica (2009), the decontaminated near-infrared CMD is not well constrained and allows alternative age and distance solutions. For assumed ages of 1 Myr and 5 Myr, they derived best-fit distances of $d = 3.9 \pm 0.4$ kpc and $d = 1.7 \pm 0.3$ kpc, respectively. Bonatto & Bica (2009) favor the further distance with an age 5 ± 4 Myr since it better accounts for the decontaminated CMD sequence. NIR photometry of the B5 star GSC00154-02384 agrees with the larger distance ($d = 4.3$ kpc) while photometry of the A2 star GSC00154-01659 agrees with the closer distance ($d = 1.4$ kpc). We note that the spectral types were estimated from optical *uvby* photometry (Philip & Egret 1980) and may be

uncertain. The A2 and B5 star are also detected in our Chandra observation as ACIS #128 and #138, respectively. Both have ~ 10 net counts, and the full-band absorption-corrected X-ray luminosities $\log L_{t,c} \sim 30 - 31$ (for $d = 1.4$ kpc) are acceptable for intermediate-mass stars, as the X-ray emission often comes from their lower-mass companions (e.g., Stelzer et al. 2005).

Getman et al. (2008b) proposed an X-ray method to determine distance to young star clusters, based on two interlocking features: X-ray luminosities of PMS stars depend on stellar mass, as seen in a wide variety of PMS populations independent of the detailed age distribution and star formation mode (Preibisch et al. 2005; Telleschi et al. 2007); and X-ray luminosities and masses scale differently with the assumed distance. We attempted this method to obtain an independent estimate of the distance to NGC 2237 using a reliable sample of bright and less obscured ($N_H < 10^{21} \text{ cm}^{-2}$) X-ray sources with $L_{t,c}$ derived in Table 3 and mass M derived from NIR photometry and Siess et al. (2000) tracks. However, comparison with the well calibrated relation $L_{t,c} = 1.99 \log M + 30.43 \text{ erg s}^{-1}$ for the Cepheus OB3b and Orion stars (Getman et al. 2006) does not provide a decisive distance for the NGC 2237 cluster: a 2 Myr old cluster at $d = 1.4$ kpc and a 5 Myr old cluster at $d = 3.9$ kpc both follow the relation with comparable scatter.

The XLFs discussed in § 4.3 are more effective and support a nearer distance. Using $d = 3.9$ kpc, the NGC 2237 XLF implies that it is a rich massive cluster $\sim 1.5 - 2$ times the population of the ONC and NGC 2244. Dozens of OB stars should be present for a standard IMF, and these are absent in the optical, NIR, and X-ray images. In addition, the X-ray-measured absorption columns are moderate, a few times 10^{21} cm^{-2} , consistent with $A_V \sim 1 - 3$ mag seen towards the central Rosette NGC 2244 cluster. For a distance $d = 3.9$ kpc along the Galactic plane, a significantly higher A_V is expected.

Therefore, we consider our choice of the near distance justified. Note that the larger distance to NGC 2237 is not ruled out by the rich population estimated from the XLF comparison; an anomalous IMF could explain the lack of OB stars. Further optical spectroscopic surveys of the NGC 2237 cluster will be invaluable to confirm whether it is a background cluster behind the Rosette region at a distance of $d = 3.9$ kpc.

5. The Global View of Star Formation Across the Complex

5.1. The Relation of NGC 2237 to NGC 2244

NGC 2237 was dubbed a twin cluster (or satellite cluster) to NGC 2244 by Li (2005), as the stellar density distribution of 2MASS sources shows a distinctive core to the west

of the compact core of NGC 2244 (see Figure 1 in Li 2005). Román-Zúñiga et al. (2008a) also identified the cluster, and pointed out that the region was historically recognized as NGC 2237. The region was not covered in the Poulton et al. (2008) *Spitzer* survey. Notably the NIR-excess disk fraction is significantly lower than those in embedded clusters (see Román-Zúñiga et al. 2008a, and Paper II), but similar to that observed in the NGC 2244 cluster.

The NGC 2237 satellite cluster is very similar in various properties – obscuration, relative location and disk fraction to the NGC 2244 cluster – to the X-ray-discovered RMC XA cluster on the eastern side of the Rosette Nebula (Paper II). The separation between NGC 2237 and the NGC 2244 cluster core is $\sim 14'$ (~ 6 pc), almost identical to the distance that separates RMC XA from NGC 2244. It is plausible that pre-existing massive molecular clumps in the natal cloud that formed NGC 2244 also collapsed and formed stars in RMC XA and NGC 2237 simultaneously with the formation of NGC 2244. However, they could also be triggered to form shortly following the onset of the HII region around the NGC 2244 O stars. Either way, these three clusters represent the early star formation episode in the Rosette complex. The stars in the three clusters are probably indistinguishable in age, and they share a similar low circumstellar disk fraction (§ 3.2). NGC 2244 clearly has the dominant OB population; NGC 2237 has many lower-mass stars but few OB stars, and RMC XA is less rich. All three clusters show substructure: a subcluster around the O5 star HD 46150 in NGC 2244 (Paper I); XA1, XA2, and XA3 in RMC XA (Paper II); and elongated structures in NGC 2237 (§ 4.2).

Further towards the west of the satellite cluster, where the molecular pillars protrude into the HII region, the ionization front from the OB stars in NGC 2244 may have triggered some star formation. These “elephant trunk” globules (Schneps et al. 1980) and bright rims (see Figure 1 and optical images of the Eagle Nebula) are commonly seen at the peripheries of many nebulae and are interpreted as illustrations of the massive star feedback into the parent molecular cloud. The evidence for triggered star formation in photoevaporating pillars is tantalizing. The alignment of the Class II sources in NGC 2237 may be a hint of an ionization front that triggered collapse along the boundary of the HII region (§ 4.2), but the number of stars involved is small. No clear evidence of an age gradient (or evolutionary sequence) is found. Dent et al. (2009) have studied the nature and mass of the small CO clumps in the Rosette including the elephant trunks/globulettes in the NGC 2237 region. They show that the globulettes are mostly low mass, which are being probably accelerated by the OB winds, and their possible age is shorter than 1 Myr. The removal of the rim gas proceeds quite rapidly, thus NGC 2237 must have emerged relatively fast from its original clump.

Only a handful of new stars are forming at the vertices of the elephant trunks in NGC 2237, perhaps fewer than the number of protostars at the tip of molecular pillars in M16 (Hester & Desch 2005). The masses of the clumps in the expanding ring range between $\sim 3\text{--}100 M_{\odot}$ (Dent et al. 2009). Star formation efficiency of a few percent will suffice to form the stars observed in the mass range of NGC 2237. Dynamical instability (Garcia-Segura & Franco 1996) appears to be not effective in forming stars here. As shown in Whalen & Norman (2008), expanding HII regions can either stimulate or lead to turbulent flows against the formation of later generations of stars, depending on the efficiency of cooling within the shocked material. The observed deficiency of stars forming at the ionization front here may imply that the cooling is weak and dynamical instability is not promoting formation of second-generation stars efficiently.

Note however that the paucity of X-ray stars in the pillars could be due to low sensitivity of our observation in this region. The X-ray luminosity of protostars may also be intrinsically low in the evaporating gaseous globules (EGGs): Linsky et al. (2007) report X-ray non-detection of EGGs in M16 and conclude that either the EGGs do not contain protostars or the protostars have not yet become X-ray active.

More X-ray sources are seen distributed ahead of the ionization front; these account for the density enhancement northwest of NGC 2237 seen in Figure 8. Most of these X-ray sources show hard X-ray emission, suggesting that they are embedded young stars. The presence of a likely HH object (§ 4.2) supports the ongoing formation of stars in this region. These stars may have formed as a result of interaction between the molecular materials here and the Rosette Nebula. Spectroscopy and *Spitzer* mid-IR data can determine their ages and evolutionary stages.

5.2. Large Scale Star Formation in the Rosette Complex

Figure 15a shows the *ROSAT* PSPC image with complete spatial coverage of the region revealing the brightest X-ray-emitting stars. For a high resolution comparison, we assemble our *Chandra* images (exposure corrected) in a $\sim 1.25^{\circ} \times 0.25^{\circ}$ mosaic, as shown in Figure 15b; a similar mosaic was shown by Townsley et al. (2003). The clumps of stars are apparent, which gives an overall view of their relative distributions, although the detection sensitivity is not uniform. To better understand the star formation history of this complex, we need to examine the large scale cluster formation events as an integrated process and look beyond our X-ray coverage.

To outline the relative locations of the clusters with respect to the molecular material

and the morphology of the ISM, Figure 16a shows the clusters superposed on the ^{13}CO emission map from Heyer et al. (2006). The NGC 2244 cluster has apparently expelled most of the molecular gas while creating the central cavity. The RMC XA cluster and NGC 2237 are mostly unobscured without surrounding molecular material, and the stars have low NIR-excess disk fraction. They may have formed nearly simultaneously or immediately after the formation of NGC 2244. The estimated total population is not as rich as NGC 2244, on the order of 200-600 ($\sim 10\text{-}30\%$ of the total stellar population in NGC 2244). However, their stellar masses were probably determined by the available molecular material in their parental clumps; no strong feedback that may disrupt the cloud and suppress the star formation is expected from the NGC 2244 OB stars yet as they were forming.

Moving further radially outwards, $25'\text{--}30'$ ($10 - 12$ pc) from the central OB cluster, a number of other clusters are present: RMC XB from Paper II (PL2, cluster C in Poulton et al. 2008, or structure B in Li & Smith 2005) to the southeast, PL 1 (cluster A in Poulton et al. 2008, also structure B in Li & Smith 2005) to the south, cluster REFL10 (Román-Zúñiga et al. 2008a) to the north. We also noticed a significant overdensity of stars associated with the molecular clump to the west of NGC 2237 in both the 2MASS study (see Figure 5 in Li 2005) and the FLAMINGOS NIR survey (Figure 27 in Román-Zúñiga et al. 2008a). The core is clearly seen in the CO map in Heyer et al. (2006) that shows prominent, dense molecular clumps further westwards from NGC 2237 (approximate center R.A.= $06^{\text{h}}29^{\text{m}}$, Dec.= $+05^{\circ}00'$). This cloud core was previously identified as one of the principal regions in the RMC, designated as Core E (Blitz & Thaddeus 1980). Román-Zúñiga et al. (2008a) find a collection of highly reddened NIR stars without J -band detections here. Neither *Chandra* nor *Spitzer* satellites have covered this molecular core. Nevertheless, we speculate that it could well be another region that harbors an undiscovered small embedded cluster.

As seen in Figure 16a, there is a prominent large shell-like structure in the CO map, with the above clusters located along the shell coinciding with the densest spots. Presence of such dense molecular material has been reported in other recent studies of star formation triggered by the expansion of an HII region (e.g., Deharveng et al. 2009; Kang et al. 2009). The distribution of the clusters is also simplified in the cartoon presentation in Figure 16b. These clusters could be formed through the so-called “collect-and-collapse” process (for review, see Elmegreen 1998; Deharveng et al. 2005) involving fragmentation of swept-up shells of interstellar gas by the expanding HII region of NGC 2244. When critical condensation is reached, the layers of neutral gas become gravitationally unstable and eventually fragment to form stars (Whitworth et al. 1994).

To elucidate this collect-and-collapse model, we adopt typical values in models for cloud

fragmentation induced by expanding HII regions and stellar wind bubbles (Whitworth et al. 1994). Assuming an isothermal sound speed $a_s = 0.2 \text{ km s}^{-1}$ in the shocked gas, an emitting rate of hydrogen ionizing photons $\dot{N}_{LyC} \sim 10^{49} \text{ s}^{-1}$ for the O4 and O5 stars, a wind luminosity $L_w \sim 10^{37} \text{ erg s}^{-1}$, and a hydrogen nuclei number density $n_0 \sim 1000 \text{ cm}^{-3}$ in the interstellar medium, the timescale at which fragmentation occurs is $\sim 1 - 2 \text{ Myr}$ and fragmentation starts in the shell at radii of $6 - 10 \text{ pc}$ with fragment masses around $10 - 23 M_\odot$. The ring of clusters around $10 - 12 \text{ pc}$ (RMC XB = PL 2, PL 1, and REFL 10) correspond to this predicted ring of collapsing cloud fragments. Note the presence of a massive Class I protostar (*Chandra* source #89 = IRAS 06306+0437 in Paper II) in a sparse cluster within RMC XB.

Several observations might confirm this collect-and-collapse scenario. The model predicts that active star formation, small clusters with high disk fractions, would be present in PL 1 and REFL 10 on the CO rim. The model also suggests that PL 2 formed more recently than more distant clusters in the RMC. Consistent with this prediction, Román-Zúñiga et al. (2008a) found that the IR excess fraction in PL 2 ($33\% \pm 6\%$) is higher than PL 4 ($24\% \pm 3\%$). The collect-and-collapse process that formed PL2 may be enhanced from the expansion of cluster PL4 and PL5.

We note that the four cloud fragments around the central NGC 2244 cluster form a bowl that is open towards the northeast, without significant molecular material or clusters. In this direction lies the large Monoceros Loop supernova remnant (SNR; Fountain et al. 1979; Vidal-Madjar et al. 1982; Odegard 1986), and one may speculate that it may have some influence to the RMC. However, Townsley et al. (2003) reviewed the possibility of an encounter between the SNR and the molecular cloud, and there is no sign of interaction.

Farther away from NGC 2244, the very young clusters PL4, PL5, REFL08 (together they are recognized as cluster RMC XC in Paper II, as structure C in Li & Smith 2005, and as cluster E in Poulton et al. 2008), PL6, PL7 (cluster G in Poulton et al. 2008), and REFL09 (cluster F in Poulton et al. 2008) are located along the densest mid-plane of the cloud. This was previously taken as evidence of sequentially triggered star formation (Elmegreen & Lada 1977), where one cluster provokes the formation of the next one. Based on the NIR studies of the embedded clusters, Román-Zúñiga et al. (2008a) propose a different idea of sequential formation. The IR-excess disk fraction among the clusters increases away from the nebula suggesting a rough sequence of ages, but 2 Myrs may not be enough time to produce a triggered sequence. The clusters PL7 and REFL09 are too close in age and distance to be triggered by clusters PL4 and PL5. Their formation is likely an outcome of the evolution of the primordial molecular cloud, and not from the interaction with the HII region (Román-Zúñiga et al. 2008a). In fact, recently Williams et al. (2009) show that star formation in PL06 must have been active for about 2 Myrs and still continues. This reinforces

the view that cluster formation in the RMC may have proceeded without significant time difference, except that NGC 2244 has more OB stars with powerful winds and clears its surroundings more rapidly than the other low mass star clusters (e.g., NGC 2237, REFL 10) and deeply embedded small clusters (e.g., PL 06).

6. Conclusions

We present the first high spatial resolution X-ray image of the NGC 2237 cluster in the Rosette Nebula obtained via a single *Chandra* observation, which is part of our survey of the star formation activities in the Rosette complex. Prior to this study, only 36 *K*-band excess cluster members were identified (Román-Zúñiga et al. 2008a). The effectiveness of the X-ray survey technique is clearly demonstrated. Our main findings are:

1. In this 20 ks observation, 168 X-ray point sources are detected with a limiting X-ray sensitivity of $L_t \sim 10^{30}$ ergs s⁻¹, nearly complete to the solar mass range. We associate 134 of the 168 X-ray sources with cluster stars and infer about 24 other embedded sources, giving a total of ~ 160 stellar members identified here in NGC 2237.

2. The locations of most ACIS sources in the NIR color-magnitude diagram are consistent with a small population of PMS low mass stars ($M \lesssim 2M_\odot$) in the NGC 2237 region with a visual extinction of $A_V \sim 2$ at 1.4 kpc, assuming a similar age to NGC 2244 (2 Myr old). Our X-ray sample provides the first probe of the low mass population in this satellite cluster to NGC 2244. We derive an overall *K*-excess disk frequency of 13% for stars with mass $M \gtrsim 1M_\odot$ using the X-ray-selected sample, consistent with the reported disk fraction from NIR study.

3. We examine the X-ray properties of a number of B stars in the field. Several X-ray emitting stars are located at the peripheries of pillar objects. A previously unknown optical outflow feature is seen originating inside the optically dark region, which may be a newly identified HH object; this supports the ongoing formation of stars in this region.

4. The X-ray selected population provides a reliable probe of the cluster center and structure, which agree well with previous NIR studies. Similar to RMC XA, collapse of pre-existing massive molecular clumps accompanying the formation of the NGC 2244 cluster may have formed NGC 2237 as a satellite cluster. There is tantalizing evidence suggestive of a triggered formation process in the optical dark pillars by the NGC 2244 O stars, including discovery of young Class II sources aligned in an arc and embedded hard X-ray sources across the optical Photon Dominated Region.

5. We derive the KLF and the XLF for the NGC 2237 cluster. A significant excess of stars with apparent $K_s \sim 11 - 12$ is seen in the KLF, likely associated with the presence of a few foreground stars. The slope of the NGC 2237 XLF matches the ONC XLF well, and the relative scaling implies a smaller cluster population $\sim 400-600$ for NGC 2237, which is consistent with the estimates from NIR studies. We discuss the uncertainty in the distance to NGC 2237 and prefer the near distance.

6. The large-scale star formation in the Rosette Complex is reviewed in the context of the “collect-and-collapse” scenario, given the locations of clusters and the morphology of the ISM. The formation of NGC 2244, RMC XA, and NGC 2237 represents the earliest star formation episode in the complex. The IRAS $100\mu\text{m}$ image and CO emission map show sites of currently active star formation—four potential clusters associated with the fragments of the large shell of swept-up neutral material from the expanding HII region. In the RMC, a temporal sequence of star formation across the complex is present (see Li & Smith 2005; Wang et al. 2009; Román-Zúñiga et al. 2008a). The cause of the sequence appears to be related to the molecular cloud, perhaps primordial, not limited to the originally proposed triggering scenario in Elmegreen & Lada (1977) where one cluster provokes the formation of the next one.

We thank the anonymous referee for his/her careful reading and comments that significantly improved the clarity of this paper. We thank Travis Rector and Mark Heyer for kindly providing the KPNO MOSAIC images of the Rosette Nebula and the CO emission maps of the Rosette Complex, respectively. This work was supported by the Chandra ACIS Team (G. Garmire, PI) through NASA contract NAS8-38252. E.D.F., P.S.B., and L.K.T. also received support from NASA grant NNX09AC74G. FLAMINGOS was designed and constructed by the IR instrumentation group (PI: R. Elston) at the University of Florida, Department of Astronomy with support from NSF grant AST97-31180 and Kitt Peak National Observatory. The data were collected under the NOAO Survey Program, “Towards a Complete Near-Infrared Spectroscopic Survey of Giant Molecular Clouds” (PI: E. Lada) and supported by NSF grants AST97-3367 and AST02-02976 to the University of Florida. E.A.L. also acknowledges support from NASA LTSA NNG05D66G. This publication makes use of data products from the Two Micron All Sky Survey (a joint project of the University of Massachusetts and the Infrared Processing and Analysis Center/California Institute of Technology, funded by NASA and NSF), and the SIMBAD database and the VizieR catalogue access tool (operated by the CDS).

REFERENCES

- Arnaud, K. A. 1996, in *Astronomical Society of the Pacific Conference Series*, Vol. 101, *Astronomical Data Analysis Software and Systems V*, ed. G. H. Jacoby & J. Barnes, 17
- Alter, G., Balazs, B., Ruprecht, J., & Vanysek, J. (eds.) 1970, *Catalogue of Star Clusters and Associations*, 2nd ed., Budapest: Akademiai Kiado
- Berghöfer, T. W. & Christian, D. J. 2002, *A&A*, 384, 890
- Binney, J., & Merrifield, M. 1998, *Galactic Astronomy*, Princeton University Press
- Blitz, L. & Thaddeus, P. 1980, *ApJ*, 241, 676
- Briceño, C., Preibisch, T., Sherry, W. H., Mamajek, E. A., Mathieu, R. D., Walter, F. M., & Zinnecker, H. 2007, in *Protostars and Planets V*, ed. B. Reipurth, D. Jewitt, & K. Keil, 345–360
- Broos, P. S., Townsley, L. K., Feigelson, E. D., Getman, K. V., Bauer, F. E., & Garmire, G. P. 2010, *ApJ* in press, astro-ph/1003.2397
- Broos, P. S., Feigelson, E. D., Townsley, L. K., Getman, K. V., Wang, J., Garmire, G. P., Jiang, Z., & Tsuboi, Y. 2007, *ApJS*, 169, 353
- Bonatto, C., & Bica, E. 2009, *MNRAS*, 394, 2127
- Casertano, S. & Hut, P. 1985, *ApJ*, 298, 80
- Cash, W. 1979, *ApJ*, 228, 939
- Cox, P., Deharveng, L., & Leene, A. 1990, *A&A*, 230, 181
- Deharveng, L., Zavagno, A., & Caplan, J. 2005, *A&A*, 433, 565
- Deharveng, L., Lefloch, B., Massi, F., Brand, J., Kurtz, S., Zavagno, A., & Caplan, J. 2006, *A&A*, 458, 191
- Deharveng, L., Zavagno, A., Schuller, F., Caplan, J., Pomarès, M., & De Breuck, C. 2009, *A&A*, 496, 177
- Dent, W. R. F., et al. 2009, *MNRAS*, 395, 1805
- Diggle, P. 2003, *Statistical Analysis of Spatial Point Patterns*, 2nd Edition, Hodder Arnold Publication, 2003

- Ebeling, H., White, D. A., & Rangarajan, F. V. N. 2006, MNRAS, 368, 65
- Elmegreen, B. G. 1998, in Astronomical Society of the Pacific Conference Series, Vol. 148, Origins, ed. C. E. Woodward, J. M. Shull, & H. A. Thronson, Jr., 150
- Elmegreen, B. G. & Lada, C. J. 1977, ApJ, 214, 725
- Feigelson, E. D., et al. 2005, ApJS, 160, 379
- Feigelson, E., Townsley, L., Güdel, M., & Stassun, K. 2007, in Protostars and Planets V, ed. B. Reipurth, D. Jewitt, & K. Keil, 313–328
- Feigelson, E. D., Martin, A. L., McNeill, C. J., Broos, P. S., & Garmire, G. P. 2009, AJ, 138, 227
- Freeman, P. E., Kashyap, V., Rosner, R., & Lamb, D. Q. 2002, ApJS, 138, 185
- Fountain, W. F., Gary, G. A., & Odell, C. R. 1979, ApJ, 229, 971
- Garcia-Segura, G. & Franco, J. 1996, ApJ, 469, 171
- Getman, K. V., Feigelson, E. D., Grosso, N., McCaughrean, M. J., Micela, G., Broos, P., Garmire, G., & Townsley, L. 2005, ApJS, 160, 353
- Getman, K. V., et al. 2005, ApJS, 160, 319
- Getman, K. V., Feigelson, E. D., Townsley, L., Broos, P., Garmire, G., & Tsujimoto, M. 2006, ApJS, 163, 306
- Getman, K. V., Feigelson, E. D., Garmire, G., Broos, P., & Wang, J. 2007, ApJ, 654, 316
- Getman, K. V., Feigelson, E. D., Broos, P. S., Micela, G., & Garmire, G. P. 2008, ApJ, 688, 418
- Getman, K. V., Feigelson, E. D., Lawson, W. A., Broos, P. S., & Garmire, G. P. 2008, ApJ, 673, 331
- Güdel, M., Skinner, S. L., Mel’Nikov, S. Y., Audard, M., Telleschi, A., & Briggs, K. R. 2007, A&A, 468, 529
- Hamaguchi, K., Yamauchi, S., & Koyama, K. 2005, ApJ, 618, 360
- Hensberge, H., Pavlovski, K., & Verschueren, W. 2000, A&A, 358, 553
- Herbig, G. H. 1962, ApJ, 135, 736

- Hernández, J., et al. 2007, *ApJ*, 662, 1067
- Hester, J. J. & Desch, S. J. 2005, in *Astronomical Society of the Pacific Conference Series*, Vol. 341, *Chondrites and the Protoplanetary Disk*, ed. A. N. Krot, E. R. D. Scott, & B. Reipurth, 107
- Heyer, M. H., Williams, J. P., & Brunt, C. M. 2006, *ApJ*, 643, 956
- Hillenbrand, L. A. 1997, *AJ*, 113, 1733
- Hünsch, M., Schmitt, J. H. M. M., Sterzik, M. F., & Voges, W. 1999, *A&AS*, 135, 319
- Jiang, Z., Yao, Y., Yang, J., Ando, M., Kato, D., Kawai, T., Kurita, M., Nagata, T., Nagayama, T., Nakajima, Y., Nagashima, C., Sato, S., Tamura, M., Nakaya, H., & Sugitani, K. 2002, *ApJ*, 577, 245
- Kang, M., Biegging, J. H., Kulesa, C. A., & Lee, Y. 2009, *ApJ*, 701, 454
- Koenig, X. P., Allen, L. E., Gutermuth, R. A., Hora, J. L., Brunt, C. M., & Muzerolle, J. 2008, *ApJ*, 688, 1142
- Lada, E. A., & Lada, C. J. 1995, *AJ*, 109, 1682
- Lefloch, B., & Lazareff, B. 1994, *aap*, 289, 559
- Li, J. Z. 2005, *ApJ*, 625, 242
- Li, J. Z. & Rector, T. A. 2004, *ApJ*, 600, L67
- Li, J. Z. & Smith, M. D. 2005, *A&A*, 431, 925
- Linsky, J. L., Gagné, M., Mytyk, A., McCaughrean, M., & Andersen, M. 2007, *ApJ*, 654, 347
- Monet, D. G., et al. 2003, *AJ*, 125, 984
- Moretti, A., Campana, S., Lazzati, D., & Tagliaferri, G. 2003, *ApJ*, 588, 696
- Odegard, N. 1986, *ApJ*, 301, 813
- Ogura, K., & Ishida, K. 1981, *PASJ*, 33, 149
- Ogura, K., Chauhan, N., Pandey, A. K., Bhatt, B. C., Ojha, D., & Itoh, Y. 2007, *PASJ*, 59, 199

- Pérez, M. R. 1991, *Rev. Mex. Astron. Astrofis.*, 22, 99
- Phelps, R. L. & Lada, E. A. 1997, *ApJ*, 477, 176
- Philip, A. D. & Egret, D. 1980, *A&AS*, 40, 199
- Poulton, C. J., Robitaille, T. P., Greaves, J. S., Bonnell, I. A., Williams, J. P., & Heyer, M. H. 2008, *MNRAS*, 132
- Preibisch, T., et al. 2005, *ApJS*, 160, 401
- Robin, A. C., Reylé, C., Derrière, S., & Picaud, S. 2003, *A&A*, 409, 523
- Román-Zúñiga, C. G., Elston, R., Ferreira, B., & Lada, E. A. 2008, *ApJ*, 672, 861
- Román-Zúñiga, C. G. & Lada, E. A. 2008b, in *Handbook of Star Forming Regions*, B. Reipurth (ed.), San Francisco: Astron. Soc. Pacific, in press
- Schmidt-Kaler, T. 1982, in *Landolt-Bornstein: Numerical Data and Functional Relationships in Science and Technology*, Group 6 Volume 2b Stars and Star Clusters, 451
- Schneps, M. H., Ho, P. T. P., & Barrett, A. H. 1980, *ApJ*, 240, 84
- Sicilia-Aguilar, A., Hartmann, L. W., Briceño, C., Muzerolle, J., & Calvet, N. 2004, *AJ*, 128, 805
- Siess, L., Dufour, E., & Forestini, M. 2000, *A&A*, 358, 593
- Skrutskie, M. F., et al. 2006, *AJ*, 131, 1163
- Smith, R. K., Brickhouse, N. S., Liedahl, D. A., & Raymond, J. C. 2001, *ApJ*, 556, L91
- Stelzer, B., Flaccomio, E., Montmerle, T., Micela, G., Sciortino, S., Favata, F., Preibisch, T., & Feigelson, E. D. 2005, *ApJS*, 160, 557
- Sugitani, K., Tamura, M., & Ogura, K. 1995, *ApJ*, 455, L39
- Sulentic, J. W., & Tifft, W. G. 1973, *The Revised New Catalogue of Nonstellar Astronomical Objects*, Tucson: University of Arizona Press, 1973
- Telleschi, A., Güdel, M., Briggs, K. R., Audard, M., & Palla, F. 2007, *A&A*, 468, 425
- Townsley, L. K., Feigelson, E. D., Montmerle, T., Broos, P. S., Chu, Y.-H., & Garmire, G. P. 2003, *ApJ*, 593, 874

- Townsley, L. K., Broos, P. S., Feigelson, E. D., Garmire, G. P., & Getman, K. V. 2006, *AJ*, 131, 2164
- Vidal-Madjar, A., Laurent, C., Pettini, M., Paul, J. A., & Oliver, M. 1982, Third European IUE Conference, 176, 421
- Vuong, M. H., Montmerle, T., Grosso, N., Feigelson, E. D., Verstraete, L., & Ozawa, H. 2003, *A&A*, 408, 581
- Waters, L. B. F. M., & Waelkens, C. 1998, *ARA&A*, 36, 233
- Wang, J., Townsley, L. K., Feigelson, E. D., Getman, K. V., Broos, P. S., Garmire, G. P., & Tsujimoto, M. 2007, *ApJS*, 168, 100
- Wang, J., Townsley, L. K., Feigelson, E. D., Broos, P. S., Getman, K. V., Román-Zúñiga, C. G., & Lada, E. 2008, *ApJ*, 675, 464 (Paper I)
- Wang, J., Feigelson, E. D., Townsley, L. K., Román-Zúñiga, C. G., Lada, E., & Garmire, G. 2009, *ApJ*, 696, 47 (Paper II)
- Whalen, D. J. & Norman, M. L. 2008, *ApJ*, 672, 287
- Whitworth, A. P., Bhattal, A. S., Chapman, S. J., Disney, M. J., & Turner, J. A. 1994, *MNRAS*, 268, 291
- Williams, J. P., et al. 2009, *ApJ*, 699, 1300
- Wilms, J., Allen, A., & McCray, R. 2000, *ApJ*, 542, 914
- Wolk, S. J., Harnden, Jr., F. R., Flaccomio, E., Micela, G., Favata, F., Shang, H., & Feigelson, E. D. 2005, *ApJS*, 160, 423
- Wolk, S. J., Spitzbart, B. D., Bourke, T. L., Gutermuth, R. A., Vigil, M., & Comerón, F. 2008, *AJ*, 135, 693
- Zacharias, N., Monet, D. G., Levine, S. E., Urban, S. E., Gaume, R., & Wycoff, G. L. 2005, *VizieR Online Data Catalog*, 1297, 0

Table 1. Primary *Chandra* Catalog: X-ray Source Properties

Source		Position				Extraction					Characteristics					
Seq #	CXOU J	α (deg)	δ (deg)	σ ($''$)	θ ($'$)	C_t (cts)	σ_t (cts)	B_t (cts)	C_h (cts)	PSF frac	Signif	$\log P_B$	Anom	Var	Exp (ks)	E_{med} (keV)
(1)	(2)	(3)	(4)	(5)	(6)	(7)	(8)	(9)	(10)	(11)	(12)	(13)	(14)	(15)	(16)	(17)
2	063016.82+050452.2	97.570122	5.081179	1.4	10.0	10.6	4.7	6.4	1.1	0.90	2.0	-3.4	g...	...	11.8	1.4
3	063018.34+045953.9	97.576458	4.998324	1.0	8.0	9.8	4.3	4.2	7.8	0.90	2.0	-3.9	a	15.4	4.3
4	063020.40+050351.7	97.585038	5.064382	1.2	8.7	9.2	4.3	4.8	2.4	0.90	1.9	-3.3	c	14.8	1.7
5	063022.82+045538.2	97.595104	4.927297	1.0	7.8	8.2	4.0	3.8	7.3	0.89	1.8	-3.2	a	15.4	2.6
6	063023.75+050555.8	97.598962	5.098853	0.8	9.4	36.8	7.1	6.2	30.1	0.91	4.8	<-5	g...	...	10.5	3.4
8	063025.39+050540.5	97.605833	5.094589	1.0	8.9	15.2	5.0	4.8	2.2	0.90	2.7	<-5	g...	...	11.4	1.1
10	063026.78+045341.5	97.611598	4.894866	0.9	8.1	8.1	3.7	1.9	6.5	0.77	1.9	-4.5	g...	...	13.9	2.4
11	063027.33+045347.7	97.613897	4.896602	0.8	7.9	11.5	4.3	2.5	4.1	0.85	2.4	<-5	a	14.9	1.6
12	063028.13+050530.4	97.617210	5.091779	0.8	8.3	20.7	5.5	4.3	5.1	0.90	3.4	<-5	g...	...	14.1	1.7
14	063028.66+050137.8	97.619421	5.027193	0.3	5.9	32.6	6.3	1.4	2.1	0.90	4.7	<-5	a	16.6	1.2

Note. — Table 1 is published in its entirety in the electronic edition of the *Astrophysical Journal*. A portion is shown here for guidance regarding its form and content.

Note. — **Column 1:** X-ray catalog sequence number, sorted by RA. **Column 2:** IAU designation. **Columns 3,4:** Right ascension and declination for epoch J2000.0. **Column 5:** Estimated random component of position error, 1σ , in arcseconds computed as (standard deviation of PSF inside extraction region)/ $\sqrt{(\# \text{ of counts extracted})}$. **Column 6:** Off-axis angle in arcminutes. **Columns 7,8:** Estimated net counts extracted in total energy band (0.5–8 keV) with Poisson-based standard errors. **Column 9:** Background counts extracted (total band). **Column 10:** Estimated net counts extracted in the hard energy band (2–8 keV). **Column 11:** Fraction of the PSF (at 1.497 keV) enclosed within the extraction region. Note that a reduced PSF fraction (significantly below 90%) may indicate that the source is in a crowded region. **Column 12:** Photometric significance computed as (net counts)/(upper error on net counts). **Column 13:** Log probability that extracted counts (total band) are solely from background. Some sources have P_B values above the 1% threshold that defines the catalog because local background estimates can rise during the final extraction iteration after sources are removed from the catalog. **Column 14:** Source anomalies: g = fractional time that source was on a detector (FRACEXPO from *mkarf*) is < 0.9 ; e = source on field edge; p = source piled up; s = source on readout streak. **Column 15:** Variability characterization based on the Kolmogorov-Smirnov statistic in the total band: a = no evidence for variability ($0.05 < P_{KS}$); b = possibly variable ($0.005 < P_{KS} < 0.05$); c = definitely variable ($P_{KS} < 0.005$). No value is reported for sources with fewer than 4 counts or for sources in chip gaps or on field edges. **Column 16:** Effective exposure time in ks: approximate time the source would have to be observed on axis to obtain the reported number of counts. **Column 17:** Background-corrected median photon energy (total band).

Table 2. Tentative *Chandra* Catalog: X-ray Source Properties

Source		Position				Extraction					Characteristics					
Seq. #	CXOU J	α (deg)	δ (deg)	σ ($''$)	θ ($'$)	C_t (cts)	σ_t (cts)	B_t (cts)	C_h (cts)	PSF frac	Signif	$\log P_B$	Anom	Var	Exp (ks)	E_{med} (keV)
(1)	(2)	(3)	(4)	(5)	(6)	(7)	(8)	(9)	(10)	(11)	(12)	(13)	(14)	(15)	(16)	(17)
1	063007.57+050440.7	97.531553	5.077982	1.9	11.9	9.0	5.5	14.0	0.9	0.90	1.5	-1.8	a	10.2	1.2
7	063025.18+045941.0	97.604953	4.994746	0.9	6.3	4.5	3.0	1.5	0.0	0.90	1.2	-2.3	a	16.7	1.1
9	063026.53+050240.9	97.610561	5.044707	1.1	6.8	4.0	3.0	2.0	0.5	0.89	1.1	-1.7	a	16.2	1.3
13	063028.23+045447.3	97.617645	4.913166	1.0	7.1	5.7	3.4	2.3	2.2	0.89	1.4	-2.6	g...	...	14.5	1.3
15	063028.91+045516.2	97.620469	4.921175	1.0	6.7	4.8	3.2	2.2	2.3	0.89	1.3	-2.1	a	16.6	2.1
22	063030.63+050223.4	97.627642	5.039857	0.8	5.8	4.4	3.0	1.6	3.8	0.90	1.2	-2.2	a	16.9	5.5
24	063032.45+050311.8	97.635212	5.053278	0.9	5.9	4.5	3.0	1.5	2.9	0.91	1.2	-2.3	g...	...	15.4	4.0
26	063032.75+045834.5	97.636484	4.976272	0.8	4.4	2.3	2.3	0.7	0.0	0.91	0.8	-1.5	g...	...	15.5	1.0
27	063032.83+050407.3	97.636818	5.068696	1.0	6.5	4.1	3.0	1.9	0.9	0.90	1.1	-1.9	a	15.4	1.2
29	063033.14+045704.6	97.638123	4.951299	0.8	4.8	3.3	2.5	0.7	2.5	0.89	1.0	-2.2	a	16.8	4.2

Note. — Table 2 is published in its entirety in the electronic edition of the *Astrophysical Journal*. A portion is shown here for guidance regarding its form and content.

Note. — **Column 1:** X-ray catalog sequence number, sorted by RA. **Column 2:** IAU designation. **Columns 3,4:** Right ascension and declination for epoch J2000.0. **Column 5:** Estimated random component of position error, 1σ , in arcseconds computed as (standard deviation of PSF inside extraction region)/ $\sqrt{(\# \text{ of counts extracted})}$. **Column 6:** Off-axis angle in arcminutes. **Columns 7,8:** Estimated net counts extracted in total energy band (0.5–8 keV) with Poisson-based standard errors. **Column 9:** Background counts extracted (total band). **Column 10:** Estimated net counts extracted in the hard energy band (2–8 keV). **Column 11:** Fraction of the PSF (at 1.497 keV) enclosed within the extraction region. Note that a reduced PSF fraction (significantly below 90%) may indicate that the source is in a crowded region. **Column 12:** Photometric significance computed as (net counts)/(upper error on net counts). **Column 13:** Log probability that extracted counts (total band) are solely from background. Some sources have P_B values above the 1% threshold that defines the catalog because local background estimates can rise during the final extraction iteration after sources are removed from the catalog. **Column 14:** Source anomalies: g = fractional time that source was on a detector (FRACEXPO from *mkarf*) is < 0.9 ; e = source on field edge; p = source piled up; s = source on readout streak. **Column 15:** Variability characterization based on the Kolmogorov-Smirnov statistic in the total band: a = no evidence for variability ($0.05 < P_{KS}$); b = possibly variable ($0.005 < P_{KS} < 0.05$); c = definitely variable ($P_{KS} < 0.005$). No value is reported for sources with fewer than 4 counts or for sources in chip gaps or on field edges. **Column 16:** Effective exposure time in ks: approximate time the source would have to be observed on axis to obtain the reported number of counts. **Column 17:** Background-corrected median photon energy (total band).

Table 3. X-ray Spectroscopy

Source ^a				Spectral Fit ^b			X-ray Luminosities ^c				
Seq. No.	CXOU J	$C_{t,net}$	Signif	$\log N_H$ (cm^{-2})	kT (keV)	$\log EM$ (cm^{-3})	$\log L_s$	$\log L_h$	$\log L_{h,c}$ (ergs s^{-1})	$\log L_t$	$\log L_{t,c}$
(1)	(2)	(3)	(4)	(5)	(6)	(7)	(8)	(9)	(10)	(11)	(12)
2	063016.82+050452.2	10.6	2.0	22.0 (−0.3, +0.2)	0.4	54.4(⋯, +0.3)	30.0	29.1	29.2	30.0	31.3
6	063023.75+050555.8	36.8	4.8	22.4	12.8	54.2 (−0.2, +0.2)	29.82	31.2	31.2	31.2	31.4
8	063025.39+050540.5	15.2	2.7	21.3 (⋯, +0.4)	1.0 (−0.2, +0.2)	53.5	30.2	29.5	29.5	30.3	30.5
11	063027.33+045347.7	11.5	2.4	21.9	1.2	53.6 (⋯, +0.2)	29.84	29.7	29.8	30.1	30.6
12	063028.13+050530.4	20.7	3.4	21.2 (⋯, +0.6)	2.1	53.5 (−0.3, +0.3)	30.1	30.1	30.1	30.4	30.5
14	063028.66+050137.8	32.6	4.7	21.9	0.6 (−0.3, +0.7)	54.3 (⋯, +1.0)	30.3	29.6	29.7	30.4	31.3
16	063028.95+050512.4	10.3	2.1	20.4	5.8	53.2	29.9	30.1	30.1	30.3	30.3
17	063029.28+050113.2	9.8	2.2	22.1	10.7	53.3	29.3	30.3	30.4	30.3	30.5
19	063029.51+050053.1	11.7	2.5	22.1 (⋯, +0.5)	1.1	−5.8	29.29	30.5	30.5	30.5	30.6
20	063030.14+045949.3	14.1	2.8	23.0 (−0.3, +0.4)	3.4	54.3 (⋯, +1.3)	⋯	30.7	31.1	30.7	⋯

^aCols. (1)–(4) reproduce the source identification, net counts, and photometric significance data from Table 1.

^bCols. (5) and (6) present the best-fit values for the extinction column density and plasma temperature parameters. In four cases (#19, 113, 162 and 163), a powerlaw spectral model gives a significantly better fit than a single-temperature thermal model. In these cases, column (6) gives the powerlaw index Γ and column (7) gives the normalization of the spectrum in italics. Col. (7) presents the emission measure derived from the model spectrum, assuming a distance of 1.4 kpc. Quantities marked with an asterisk (*) were frozen in the fit. Uncertainties represent 90% confidence intervals. More significant digits are used for uncertainties < 0.1 in order to avoid large rounding errors; for consistency, the same number of significant digits is used for both lower and upper uncertainties. Uncertainties are missing when XSPEC was unable to compute them or when their values were so large that the parameter is effectively unconstrained. Fits lacking uncertainties, fits with large uncertainties, and fits with frozen parameters should be viewed merely as splines to the data to obtain rough estimates of luminosities; the listed parameter values are unreliable.

^cX-ray luminosities derived from the model spectrum are presented in cols. (8)–(12): (s) soft band (0.5–2 keV); (h) hard band (2–8 keV); (t) total band (0.5–8 keV). Absorption-corrected luminosities are subscripted with a *c*. Cols. (8) and (12) are omitted when $\log N_H > 22.5 \text{ cm}^{-2}$ since the soft band emission is essentially unmeasurable.

Table 4. Stellar Counterparts

X-ray Source		Optical/Infrared Photometry									
Seq	CXOU J	USNO B1.0	B	R	I	2MASS	FLAMINGOS	J	H	K	PhCcFlg
#		ID	(mag)	(mag)	(mag)	ID	ID	(mag)	(mag)	(mag)	
(1)	(2)	(3)	(4)	(5)	(6)	(7)	(8)	(9)	(10)	(11)	(12)
1	063007.57+050440.7	06300735+0504423	063007+050442	14.12	13.26	12.89	AAA000
2	063016.82+050452.2	0950-0096116	20.03	17.53	16.05	06301680+0504518	063016+050452	14.52	13.74	13.42	AAA000
3	063018.34+045953.9
4	063020.40+050351.7	0950-0096157	20.41	...	16.90	06302046+0503528	063020+050352	15.04	14.25	13.89	AAA000
5	063022.82+045538.2	063022+045539	...	18.36	17.43
6	063023.75+050555.8
7	063025.18+045941.0	0949-0093548	20.41	18.04	16.33	06302519+0459412	063025+045941	14.80	14.20	13.86	AAA000
8	063025.39+050540.5	0950-0096215	18.79	16.75	15.39	06302550+0505402	063025+050540	13.89	13.15	12.81	AAA000
9	063026.53+050240.9	0950-0096223	...	18.50	17.32	06302649+0502411	063026+050241	15.61	14.74	14.37	AAA000
10	063026.78+045341.5	063026+045344	...	18.22	17.45

Note. — Table 4 is published in its entirety in the electronic edition of the *Astrophysical Journal*. A portion is shown here for guidance regarding its form and content.

Note. — The errors of the *BRI* magnitudes are < 0.02 mag in general for stars $V < 17$ mag and become > 0.05 mag for fainter stars $V > 19$ mag (Berghöfer & Christian 2002). The mean photometric uncertainties in FLAMINGOS are 0.058 ± 0.012 , 0.064 ± 0.018 , and 0.056 ± 0.014 for J, H, and K, respectively (Román-Zúñiga et al. 2008a). The typical errors are much smaller for brighter stars (e.g., $\sigma_J = 0.02$ mag for stars with $J < 16$ mag). For 2MASS photometric quality flags, see Cutri et al. (2003).

Note. — **Columns 1–2** reproduce the sequence number and source identification from Table 1 and Table 2. For convenience, [OI81]=Ogura & Ishida (1981), [MJD95]=Massey, Johnson, & Degioia-Eastwood (1995), [BC02]=Berghöfer & Christian (2002)

⁵³= [OI81] 14 = [MJD95] 104; spectral type B1V; pmRA=11.0 mas/yr, pmDE=-2.8 mas/yr

⁵⁴= [OI81] 10 = [MJD95] 108; spectral type B2V; pmRA=-2.3 mas/yr, pmDE=-11.9 mas/yr

⁶¹= V539 Mon = [OI81] 13 = [MJD95] 110=MSX6C G206.1821-02.3456; pmRA=2.8 mas/yr, pmDE=0.4 mas/yr

⁷¹= [OI81] 12 = [MJD95] 102; pmRA=6.8 mas/yr, pmDE=0.6 mas/yr

¹²⁸= [OI81] 35 = [MJD95] 471; spectral type A2;; pmRA=-0.8 mas/yr, pmDE=3.6 mas/yr

¹³⁸= [OI81] 36 = [MJD95] 497; spectral type B5; pmRA=6.5 mas/yr, pmDE=2.1 mas/yr

¹⁴¹= [MJD95] 498; pmRA=-3.0 mas/yr, pmDE=1.9 mas/yr

¹⁴⁹= [BC02] 11; known X-ray source; $\log Lx(\text{ROSAT/PSPC})=31.01 \text{ erg s}^{-1}$; pmRA=0.6 mas/yr, pmDE=-12.6 mas/yr

¹⁶¹= [MJD95] 653; pmRA=-1.0 mas/yr, pmDE=-5.4 mas/yr

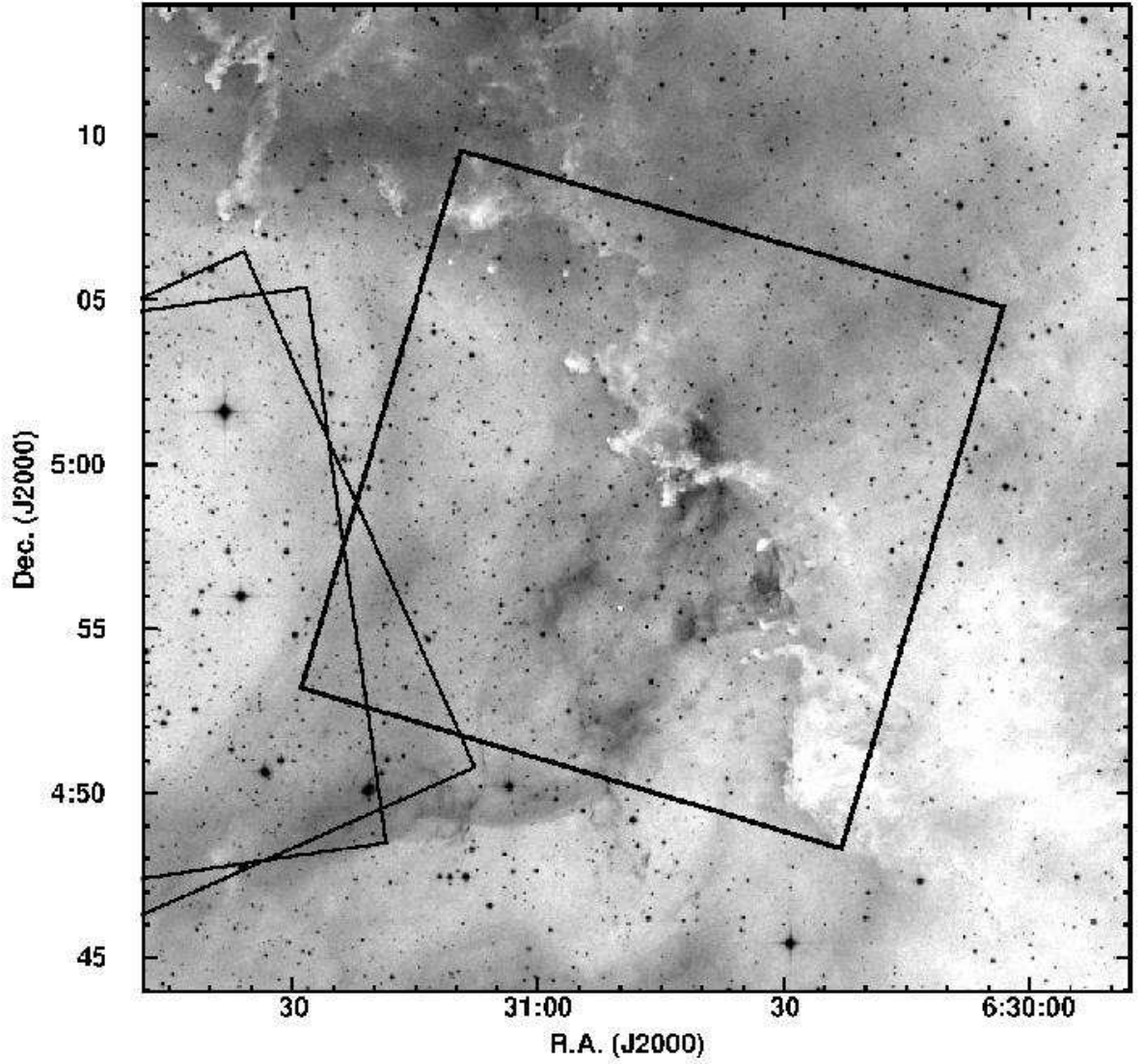


Fig. 1.— A $30' \times 30'$ DSS2 *R*-band image of the NGC 2237 region. The box outlines the $17' \times 17'$ ACIS-I field of view centered on NGC 2237. The fields to the east outline the deeper exposures of the rich NGC 2244 cluster at the center of the Rosette Nebula presented in Paper I.

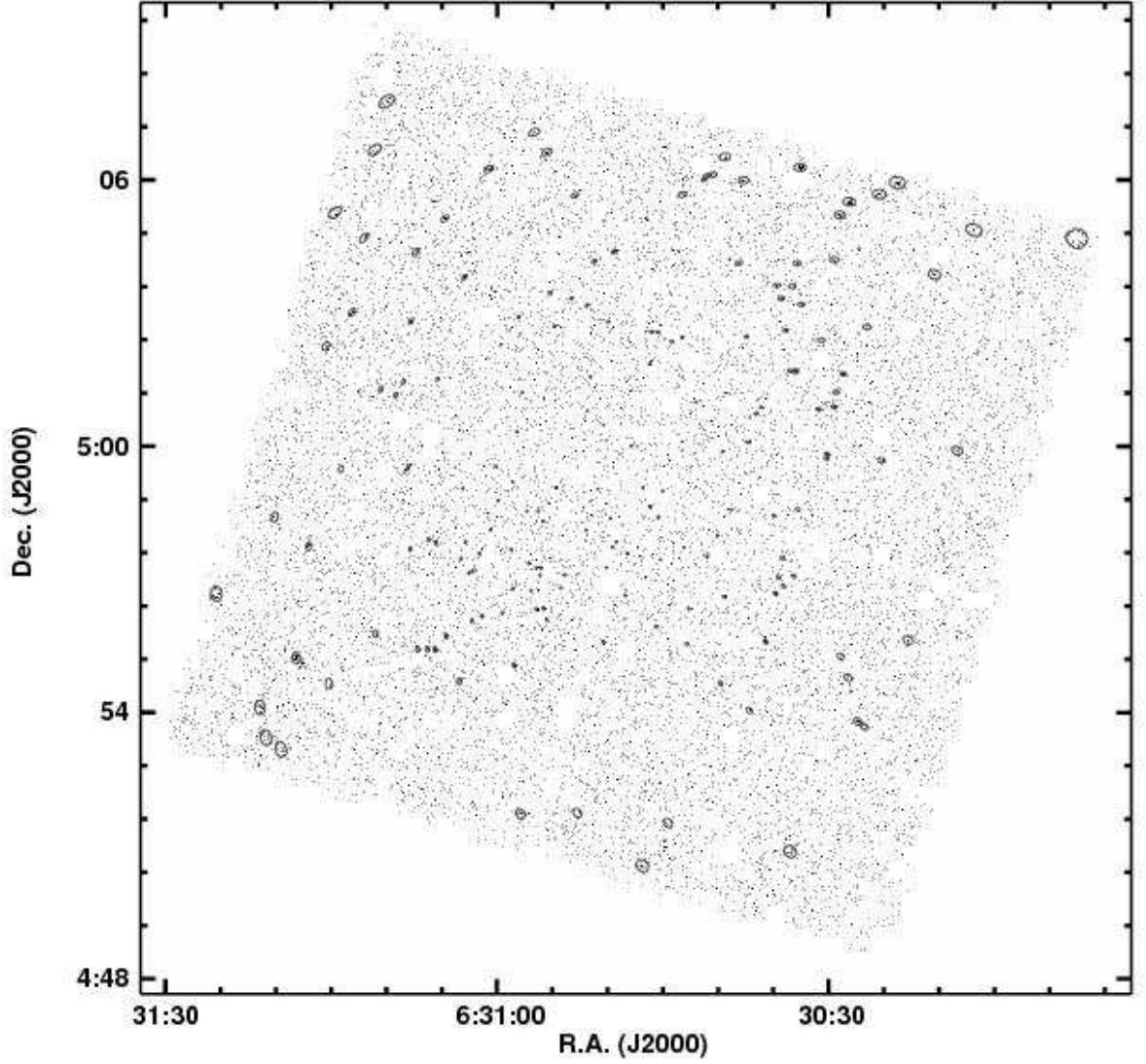


Fig. 2.— *Chandra* ACIS-I image of the NGC 2237 region (0.5-8 keV) overlaid with 168 source extraction regions. The source extraction region is based on the local PSF, enclosing approximately 90% of the PSF at 1.49 keV.

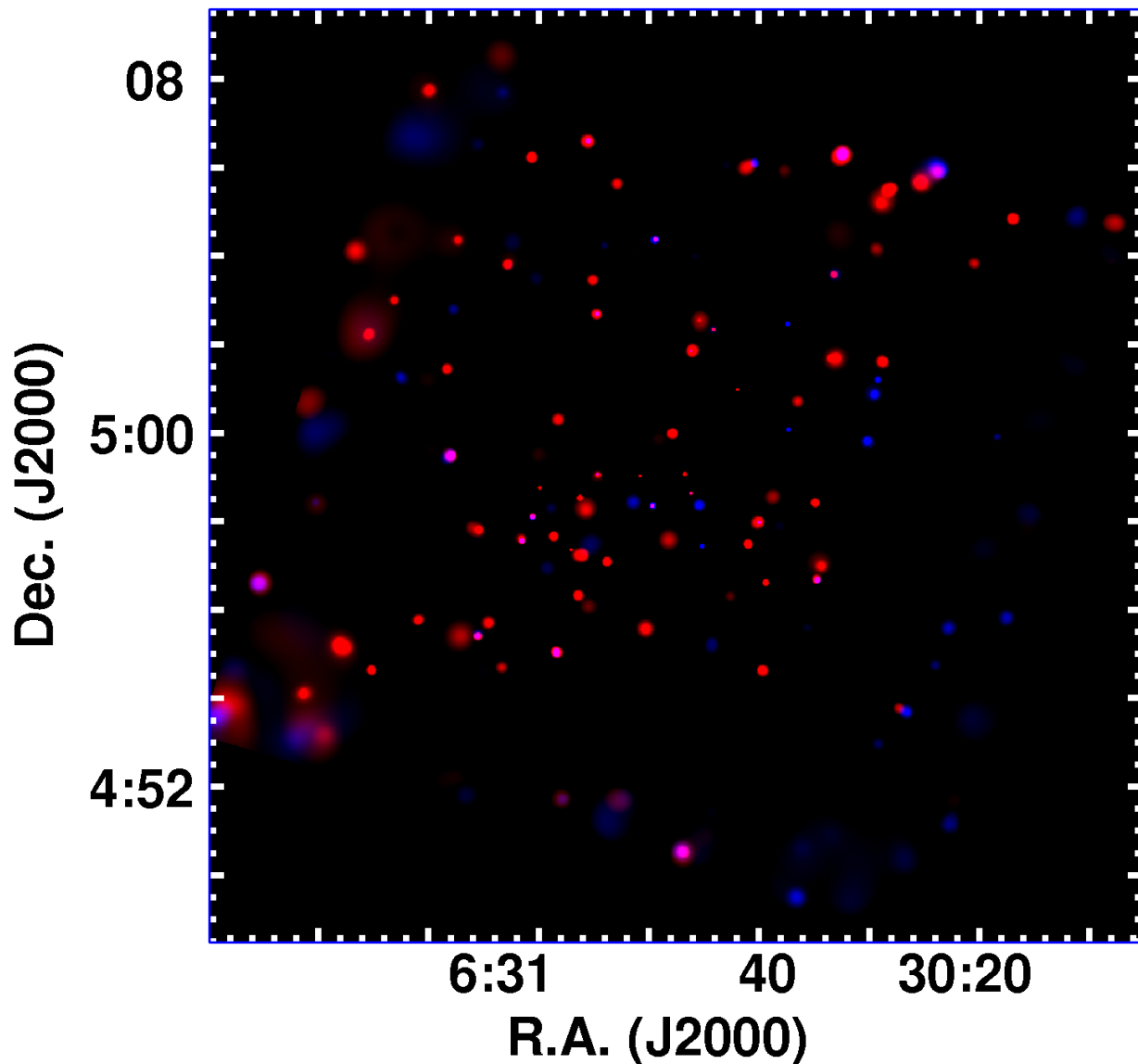


Fig. 3.— Adaptively smoothed, exposure corrected ACIS-I image of the NGC 2237 region where red represents soft X-ray emission (0.5–2 keV) and blue represents hard X-ray emission (2–7 keV). Red sources are stars with emission dominated by soft counts. Sources near the field edge appear larger due to optical distortion of the *Chandra* mirrors.

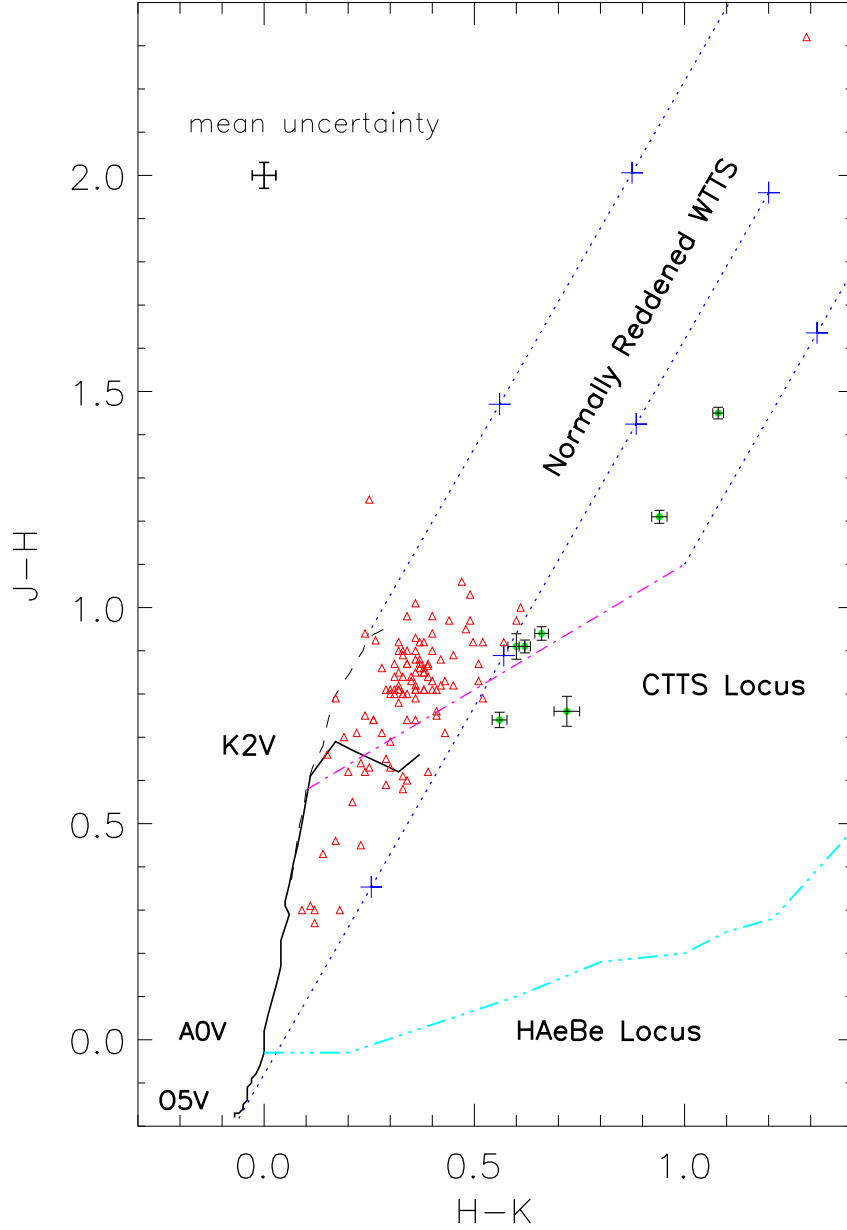


Fig. 4.— NIR $J - H$ vs. $H - K$ color-color diagram for *Chandra* stars with high-quality JHK photometry. The green circles and red triangles represent sources with and without significant K -band excess. The black solid and long-dash lines denote the loci of MS stars and giants, respectively, from Bessell & Brett (1988). The purple dash dotted line is the locus for classical T Tauri stars from Meyer et al. (1997), and the cyan solid line is the locus for Herbig Ae/Be stars from Lada & Adams (1992). The blue dashed lines represent the standard reddening vector with crosses marking every $A_V = 5$ mag. The weak-line T Tauri stars are located in the domain between the blue dashed lines indicated as the WTTS locus.

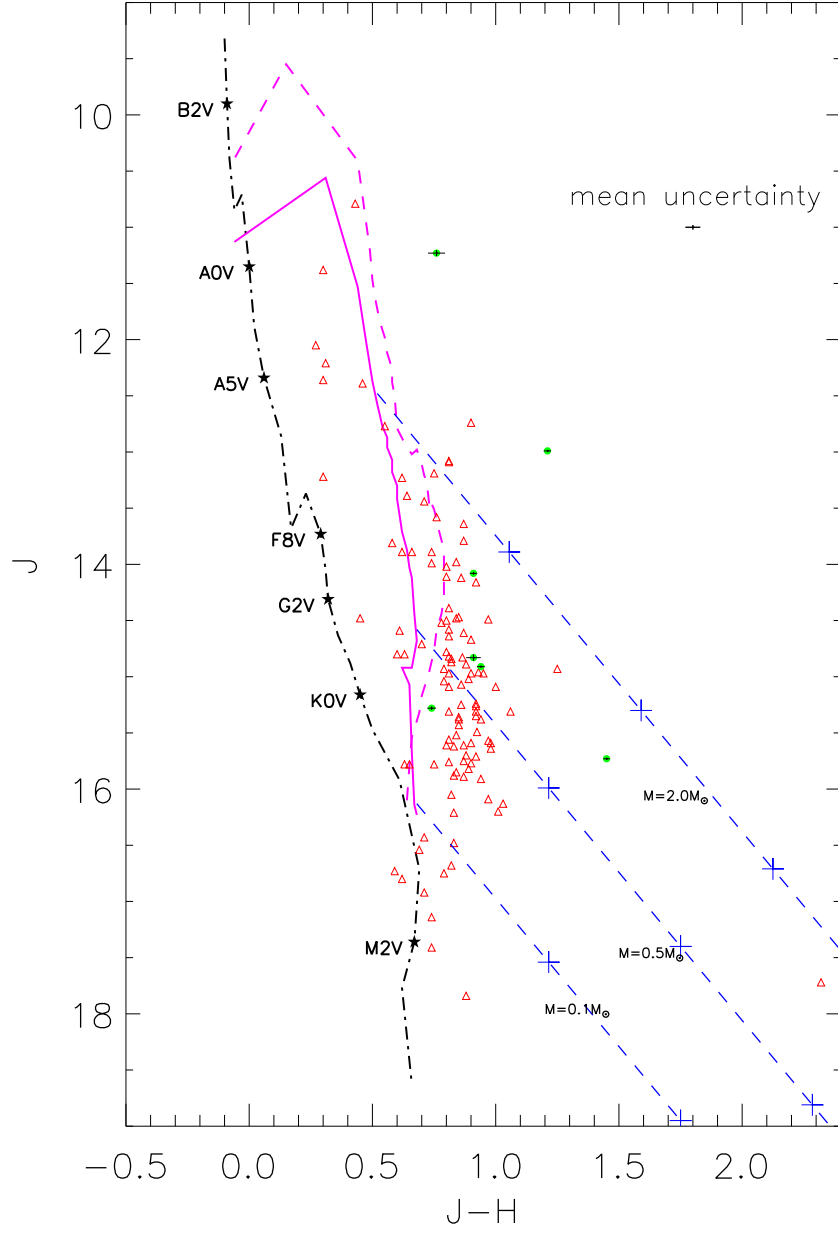


Fig. 5.— NIR J vs. $J-H$ color-magnitude diagram using the same sample and symbols as Figure 4. The purple solid line and dashed line are the 2 Myr isochrone and the 1 Myr isochrone for PMS stars from Siess et al. (2000), respectively. The dash dotted line marks the location of Zero Age Main Sequence (ZAMS) stars. The blue dashed lines represent the standard reddening vector with crosses marking every $A_V = 5$ mag and the corresponding stellar masses are marked.

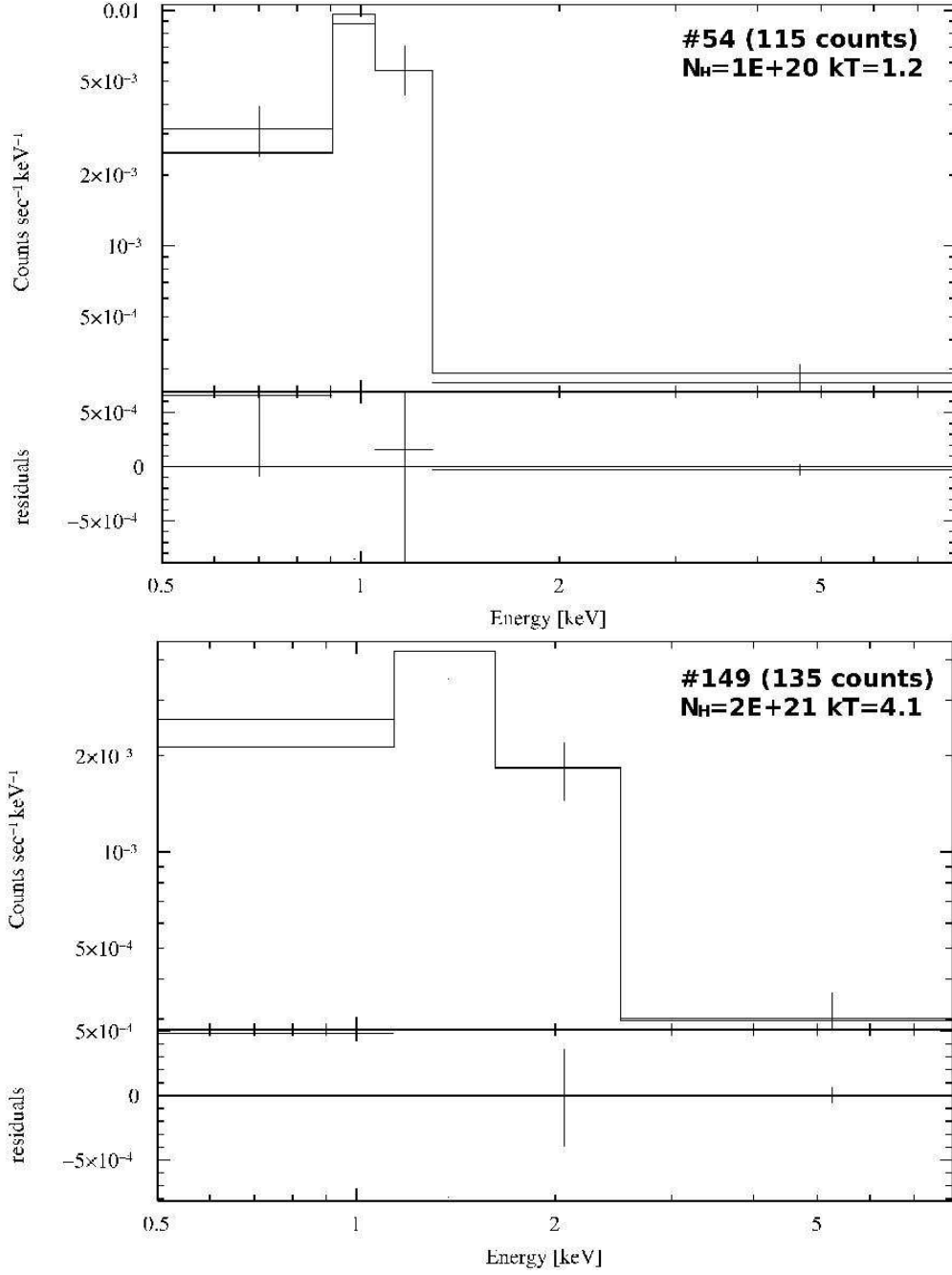


Fig. 6.— (a) The X-ray spectrum and the spectral fit for the second brightest X-ray source in the field (#54). (b) The X-ray spectrum and the spectral fit for the brightest X-ray star (#149) in the field. See text for the best-fit model parameters.

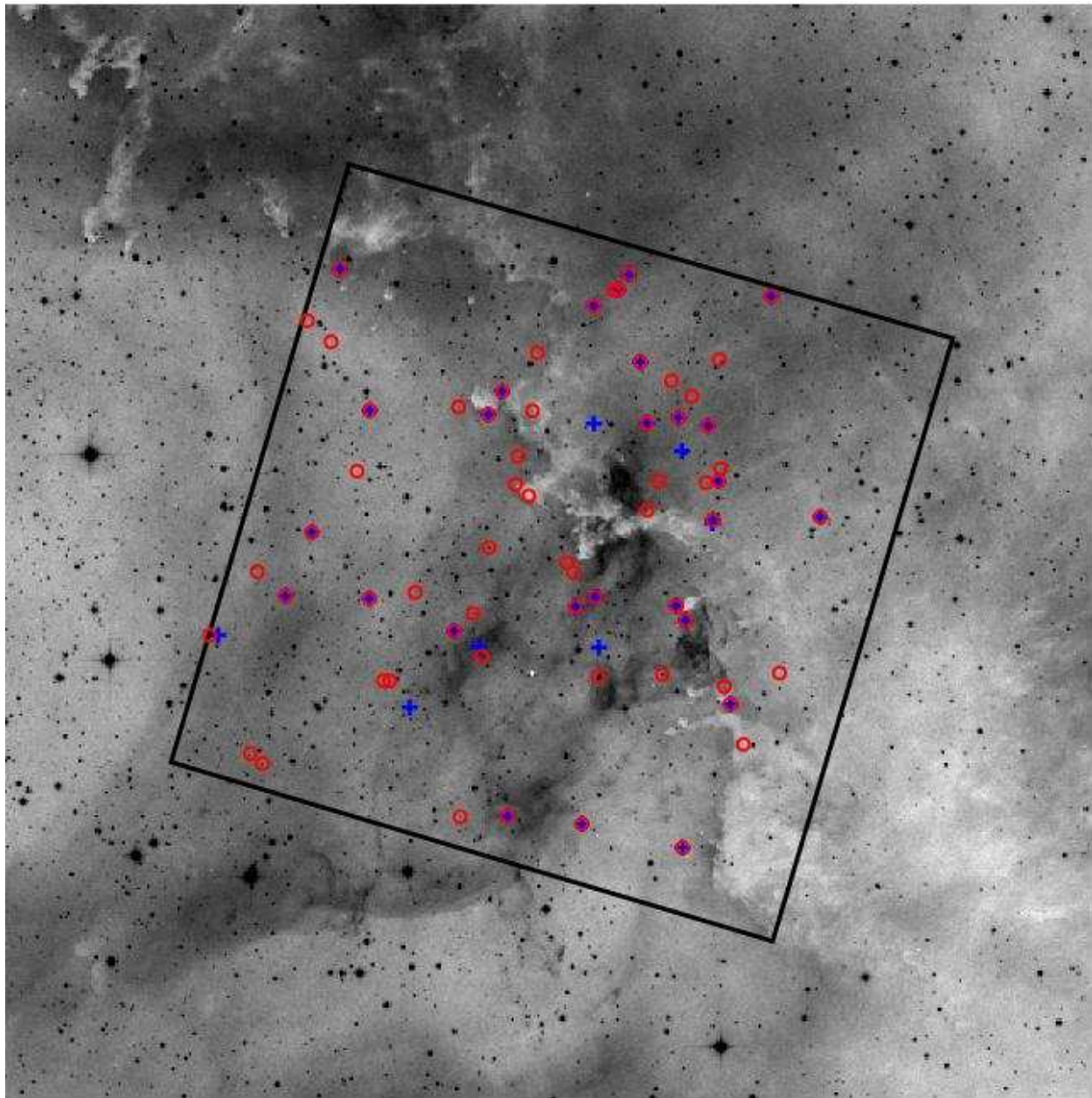


Fig. 7.— The spatial distribution of X-ray sources that do not have matched IR counterparts (shown as blue crosses) and sources that have hard median photon energies ($MedE > 2.0$ keV; shown as red circles). About ten hard X-ray sources without matched NIR counterparts are located inside the HII region cavity; these are likely AGNs. The rest, located inside the optical dark pillar region, are probably embedded young stars.

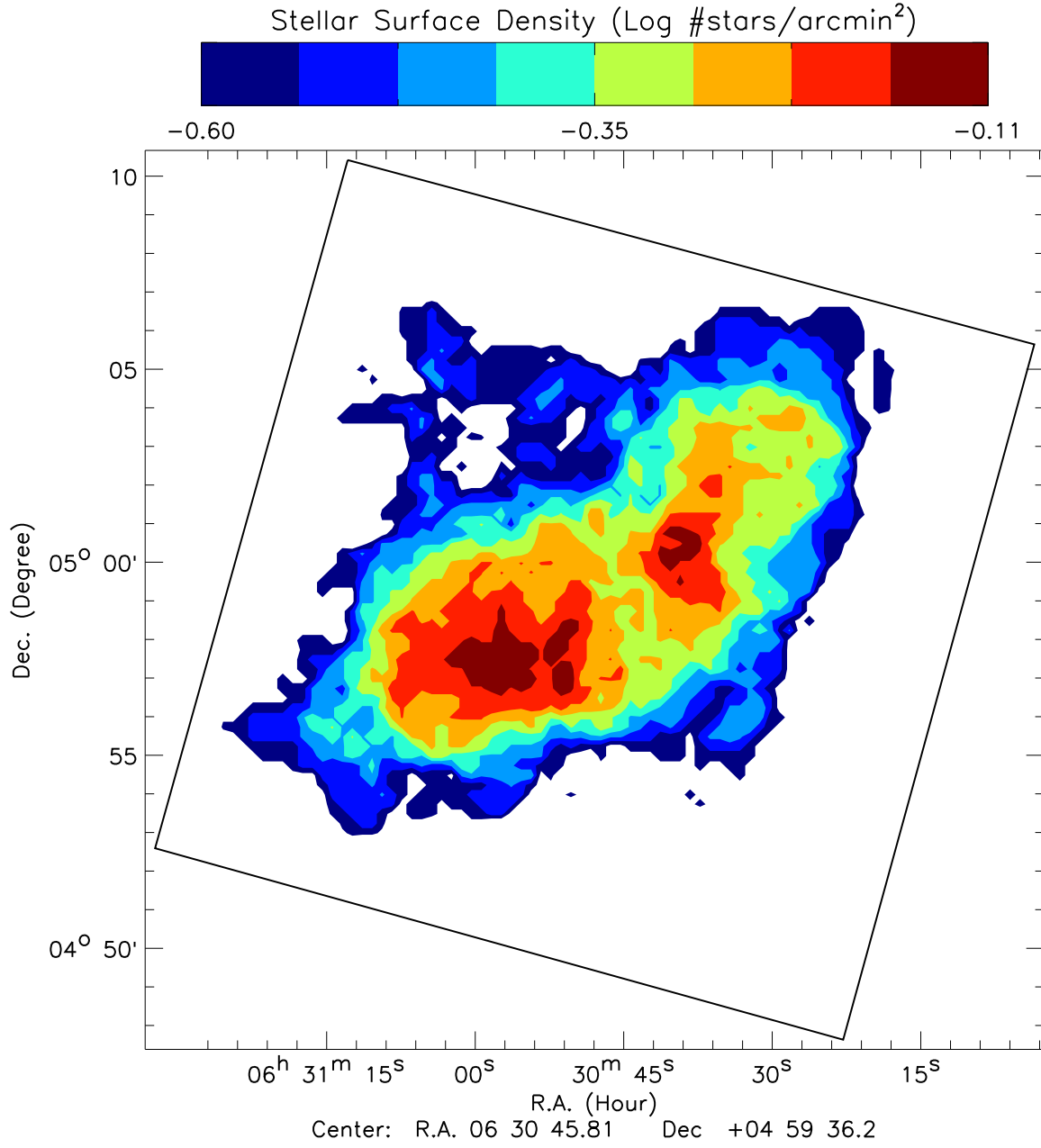


Fig. 8.— Map of the stellar surface density, in units of log stars per arcmin², for NGC 2237 sources with 6 or more net counts. It is smoothed with a 1.5' radius sampling kernel.

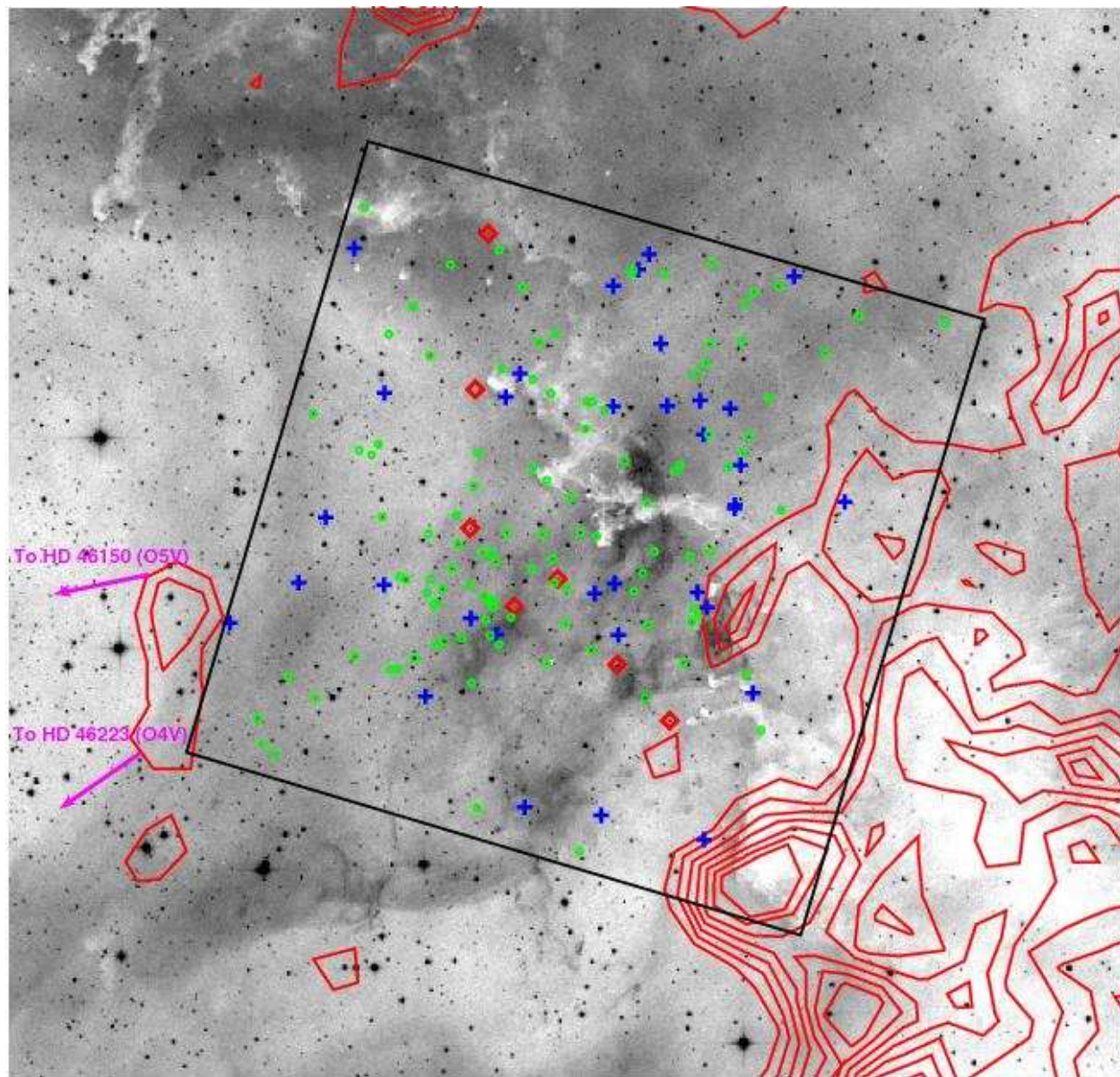


Fig. 9.— The spatial distribution of the X-ray sources superposed on the optical DSS image. The X-ray-selected stars are Class II (red diamonds) and Class III (green circles) based on their NIR colors. Some X-ray sources without NIR counterparts (blue plusses) are likely embedded stars. The molecular gas is outlined by the contours (red) from the ^{12}CO emission survey of Heyer et al. (2006).

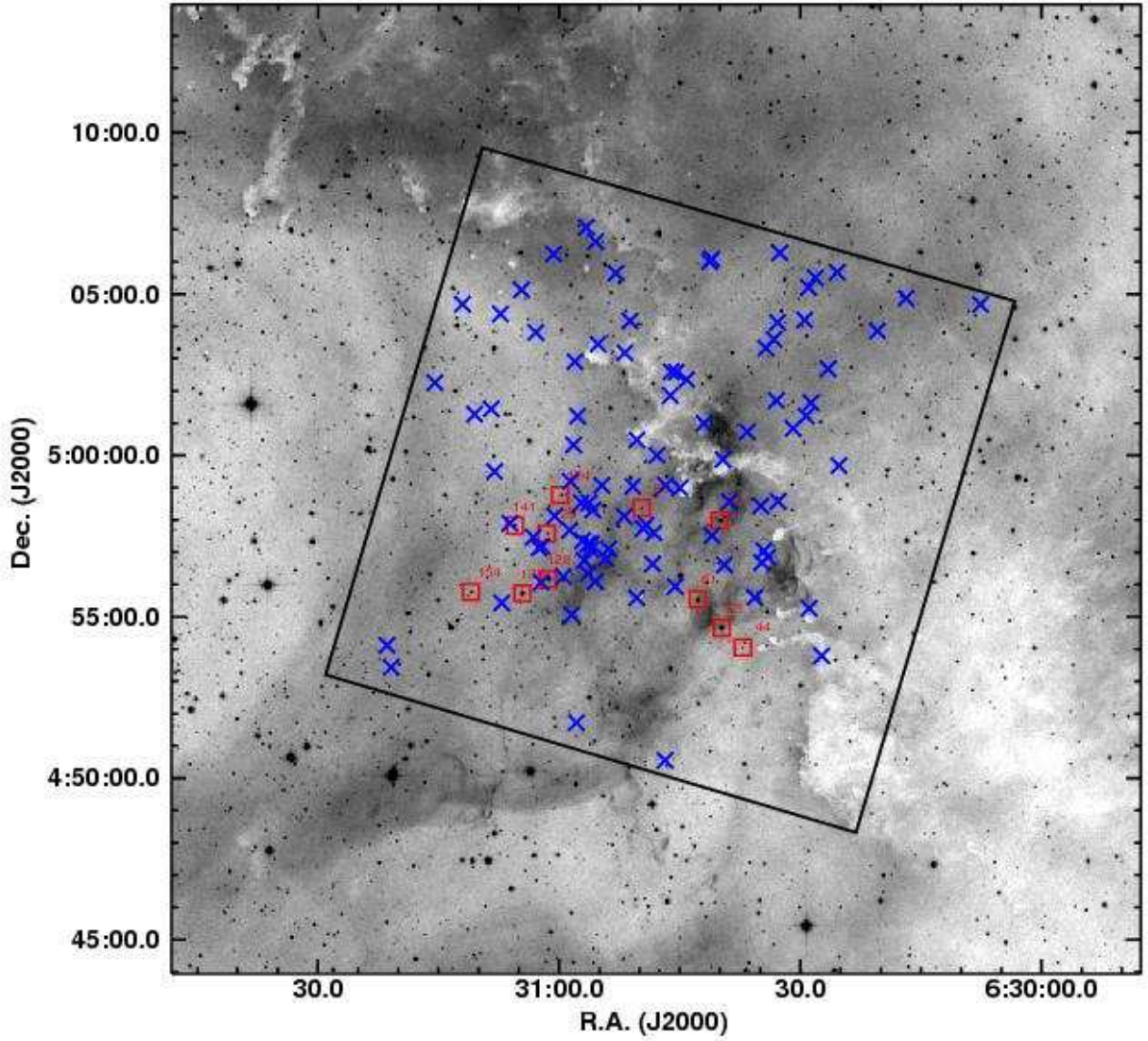


Fig. 10.— Mass-stratified spatial distribution of NGC 2237 stars: $M \gtrsim 2M_{\odot}$ (red boxes), and $M < 2M_{\odot}$ (blue crosses). Masses are based on identified spectral types or estimated from NIR photometry.

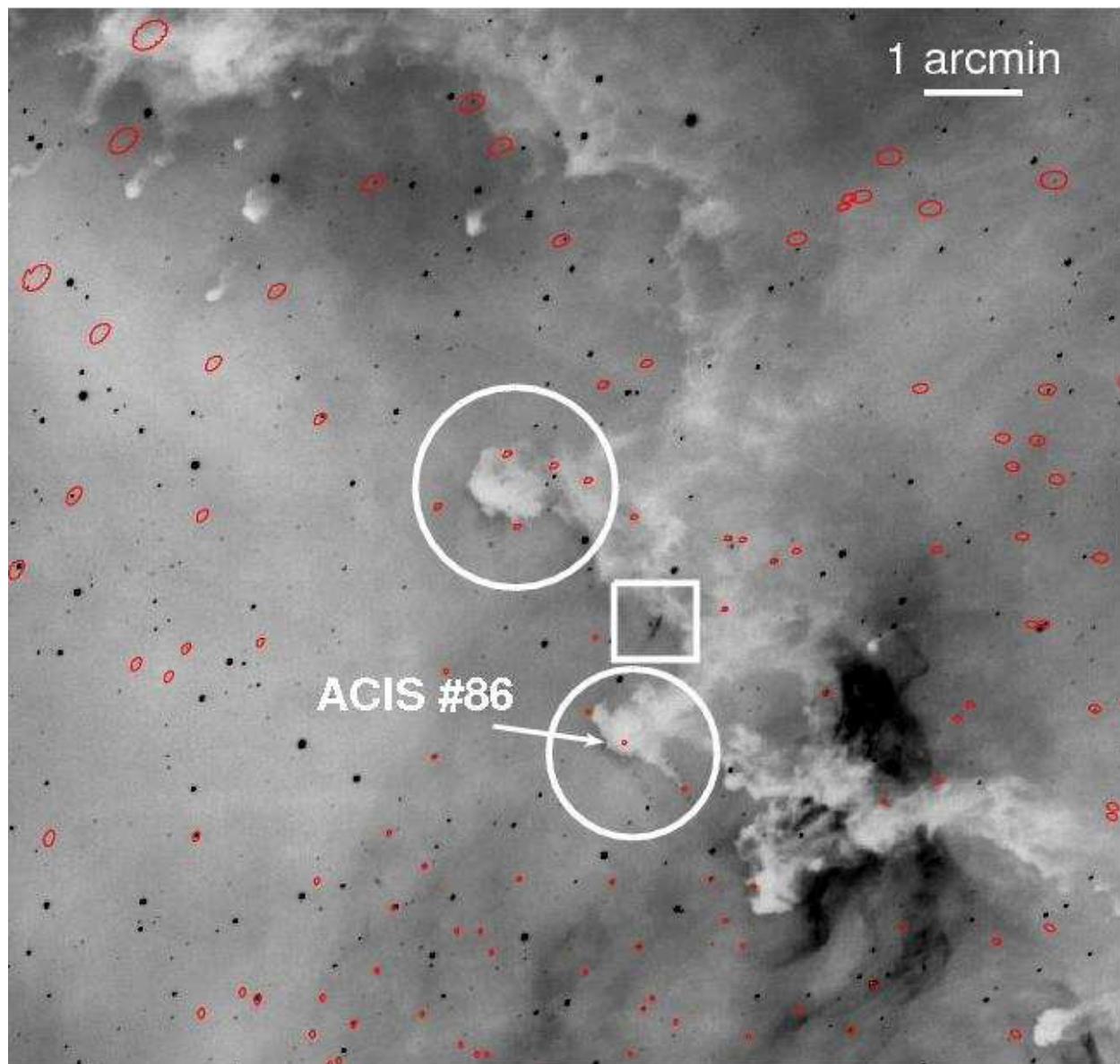


Fig. 11.— The KPNO $H\alpha$ image of a region on the interface between the cloud and ionized nebula. Extraction regions of X-ray sources are shown in red. Two optically dark pillar objects are circled. Source #86 (only 4 net counts) appears highly obscured with a visual extinction of ~ 20 mag in the NIR diagrams, possibly a star embedded in or behind the dense pillar. A likely Herbig-Haro object is marked with a box.

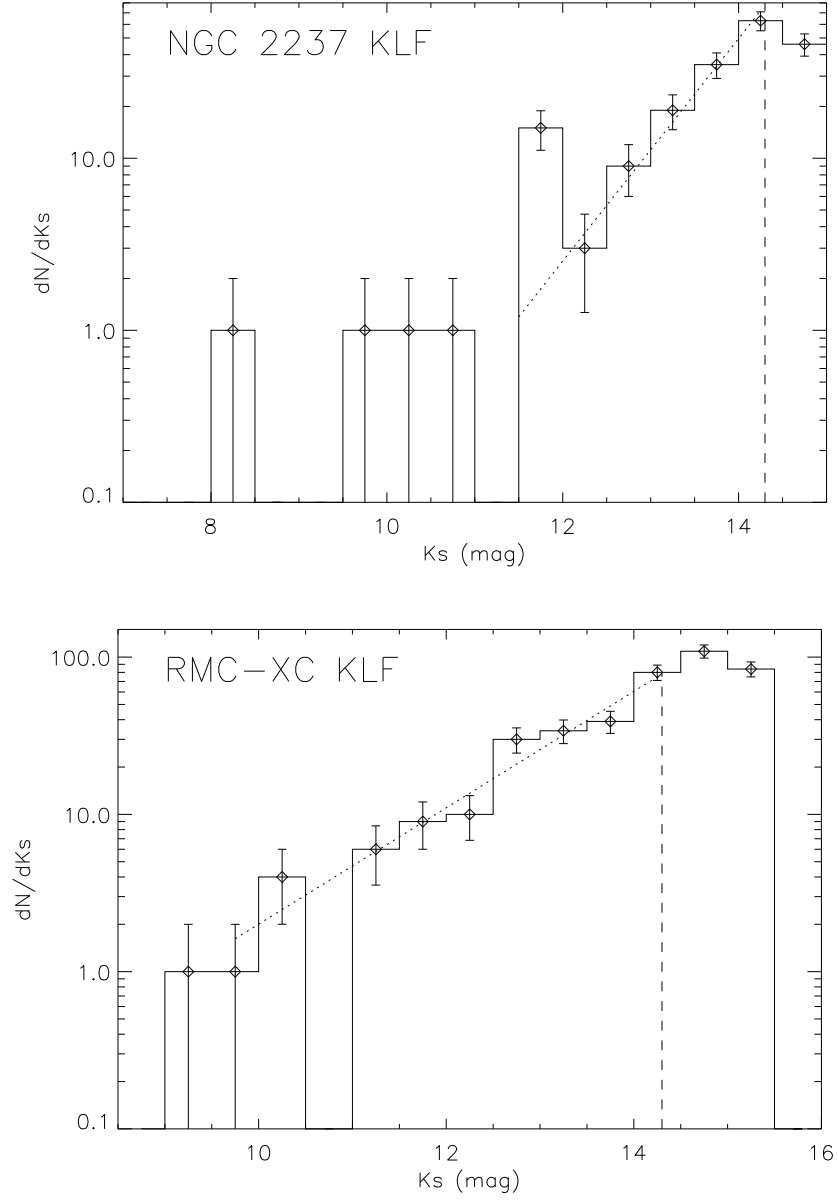


Fig. 12.— (a) The K_s -band luminosity function of NGC 2237 after correction for reddening (assuming $A_V = 2.5$ mag) and background contamination. The KLF is found to match a power-law distribution with a slope of 0.6 (dotted line). The vertical dashed line indicates the 2MASS K_s band completeness limit. (b) The KLF for cluster RMC XC (assuming $A_V = 8$ mag; Román-Zúñiga et al.2008a). The power-law slope here is 0.39.

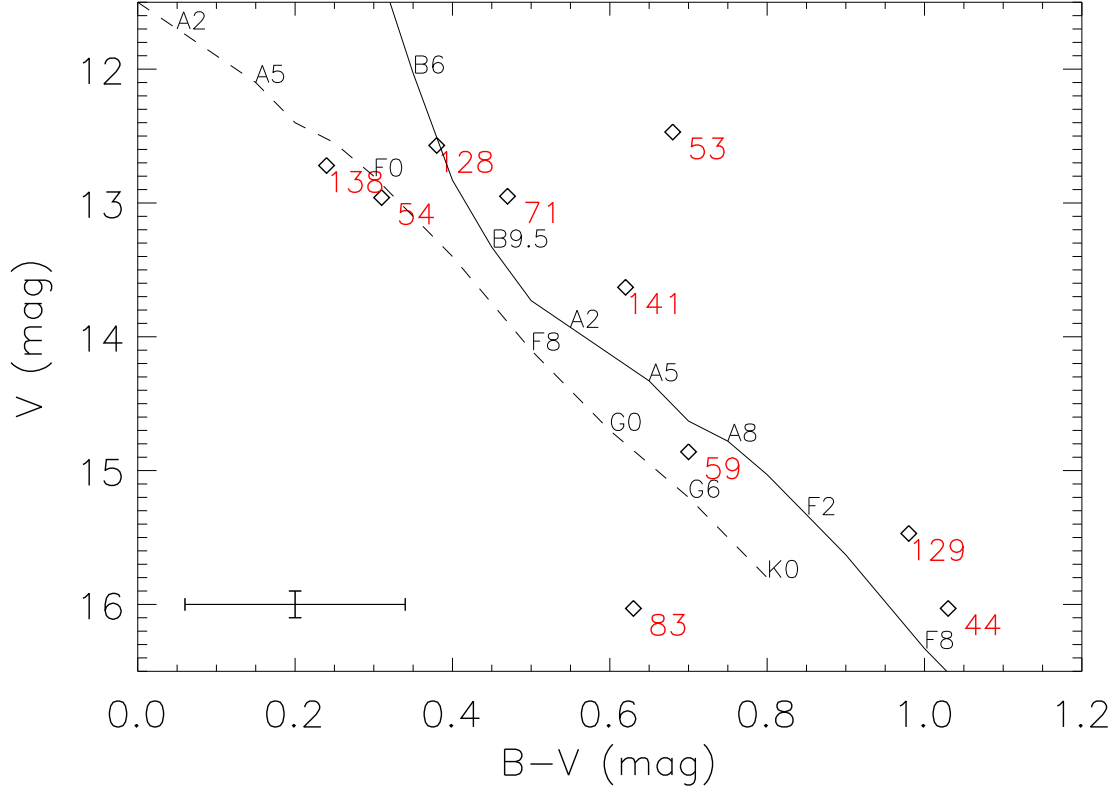


Fig. 13.— The optical CMD for the 10 X-ray detected K-band bright sources, with ACIS source sequence numbers labeled. The solid line shows the zero-age main sequence (ZAMS) isochrone (Schmidt-Kaler 1982) assuming a reddening of $E(B - V) = 0.5$ and a distance of $d = 1.4$ kpc, whereas the dashed line represent the ZAMS location for foreground stars at 1 kpc with no reddening. The typical error bars for the photometry are shown.

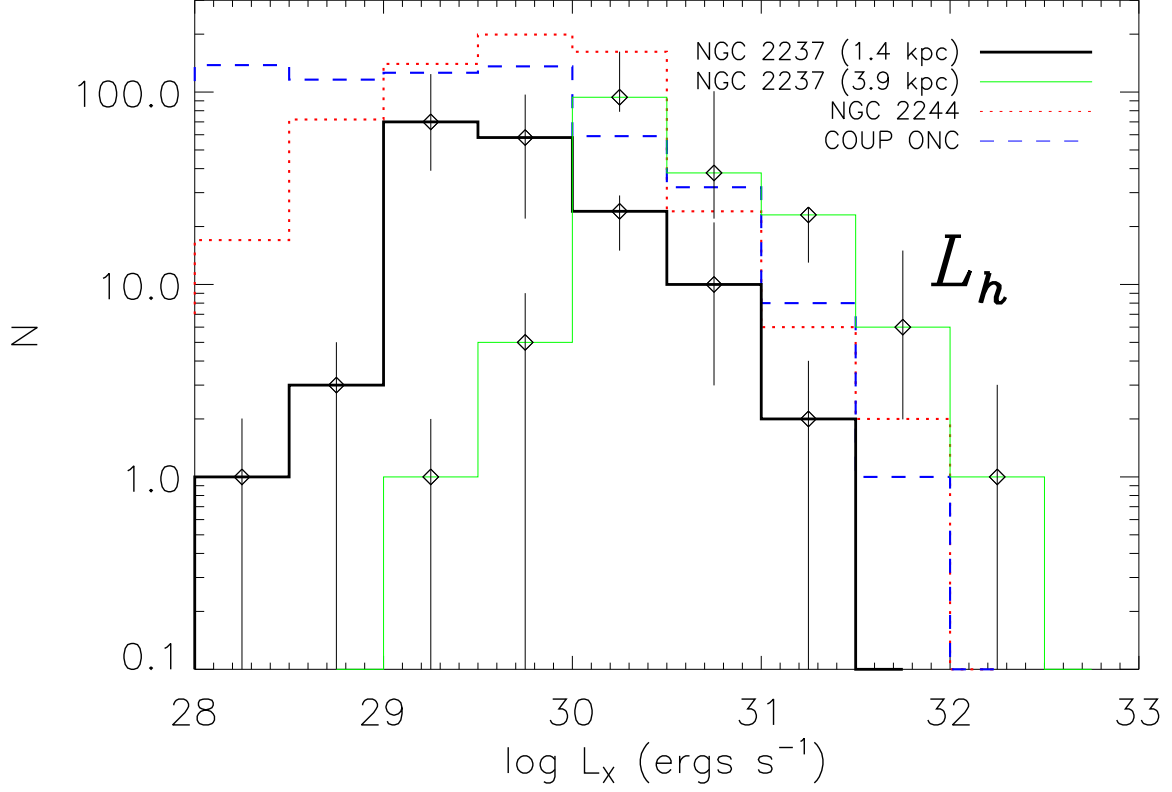


Fig. 14.— The hard band (2-8 keV) X-ray luminosity function of NGC 2237 (black solid line). For comparison, the XLFs for NGC 2244 (red dotted line) and the COUP ONC (blue dashed line) are plotted. The XLF derived using a farther distance $d = 3.9$ kpc (green solid line) is also shown.

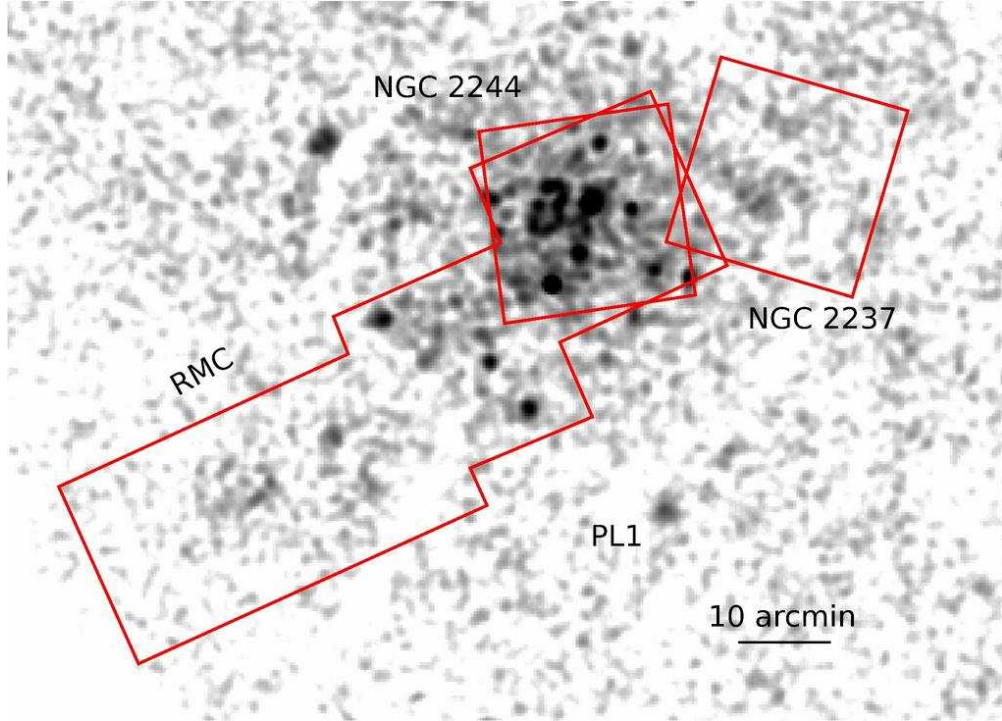
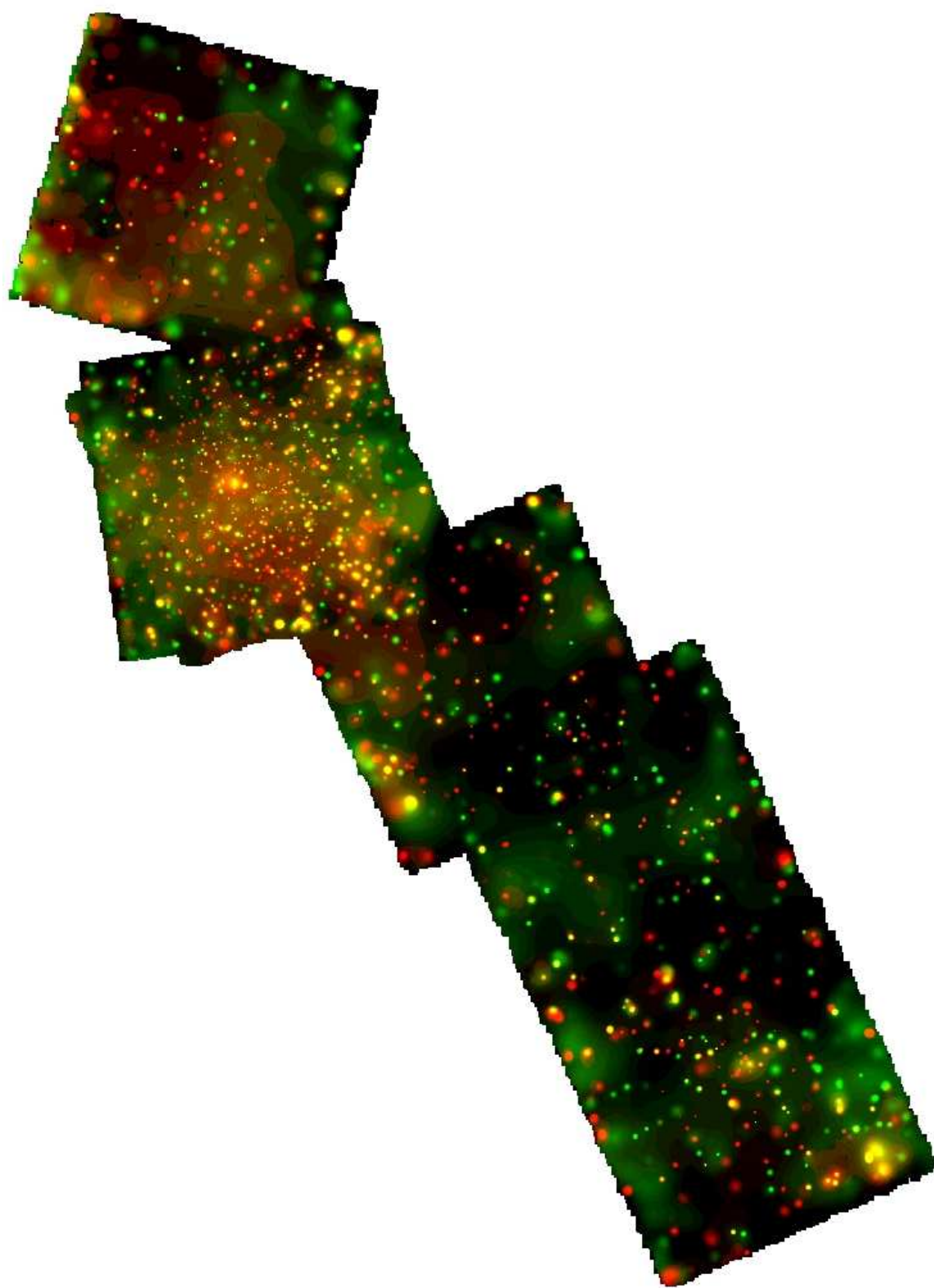


Fig. 15.— (a) *ROSAT* PSPC image of the Rosette Complex with existing Chandra pointings outlined by the red boxes. (b) *Chandra* ACIS-I mosaic of six observations in the Rosette Complex. Red represents soft band (0.5–2 keV) X-ray emission, and green represents hard band (2–7 keV) X-ray emission. The Chandra image is rotated for better layout in the page; the actual orientation is the same as (a), where north is up and east is to the left. A similar image without the NGC 2237 exposure is shown by Townsley et al. (2003).



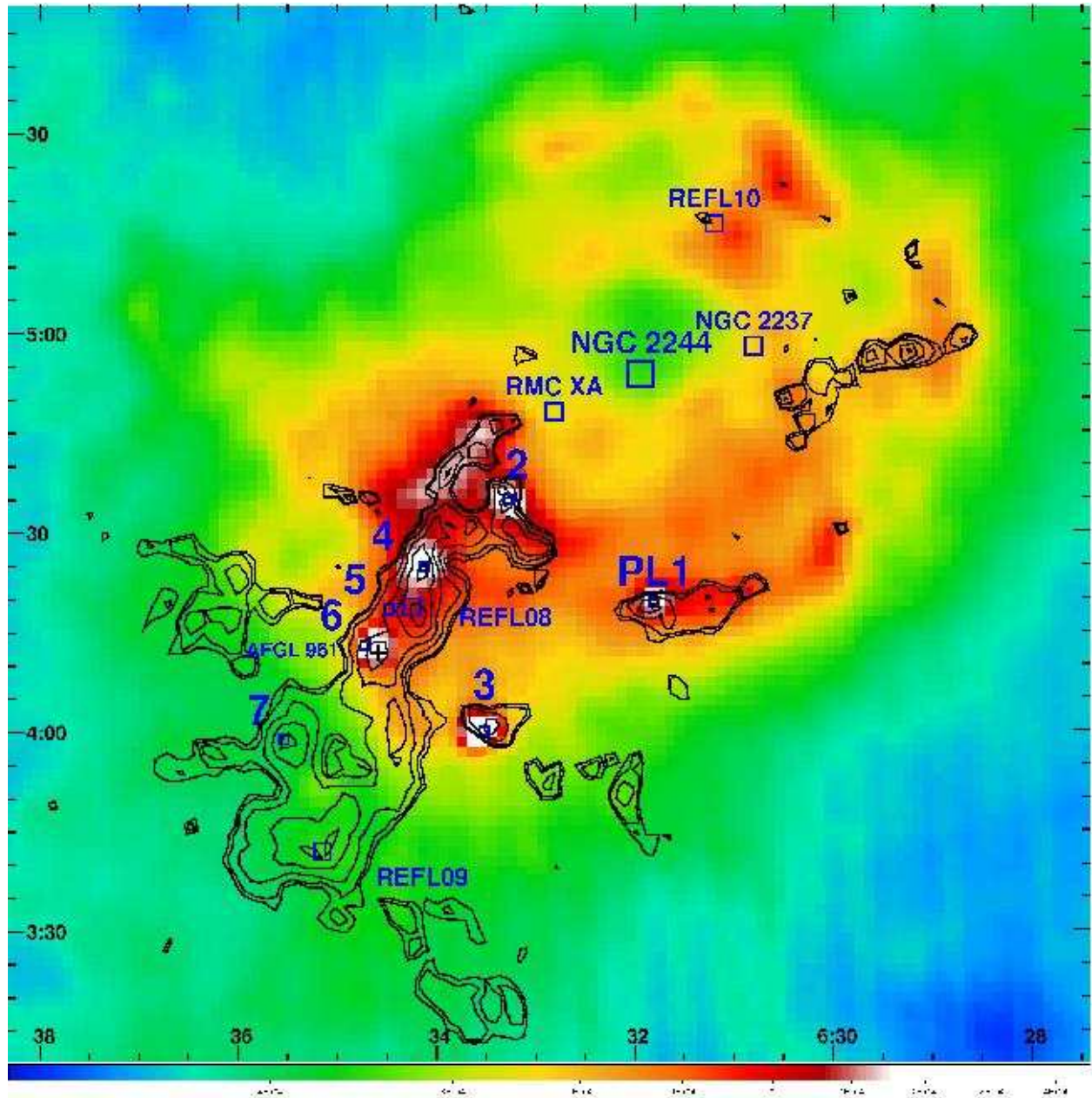


Fig. 16.— (a) A large scale view of the Rosette Complex using the $100\mu\text{m}$ IRAS map shown in color. ^{13}CO emission contours from Heyer et al. (2006) are overlaid. Previously identified clusters from Phelps & Lada (1997), Román-Zúñiga et al. (2008a), and Wang et al. (2009) are labeled. (b) A cartoon presentation of (a) with the dark clouds and nearby supernova remnant outlined and the clusters marked with stars.

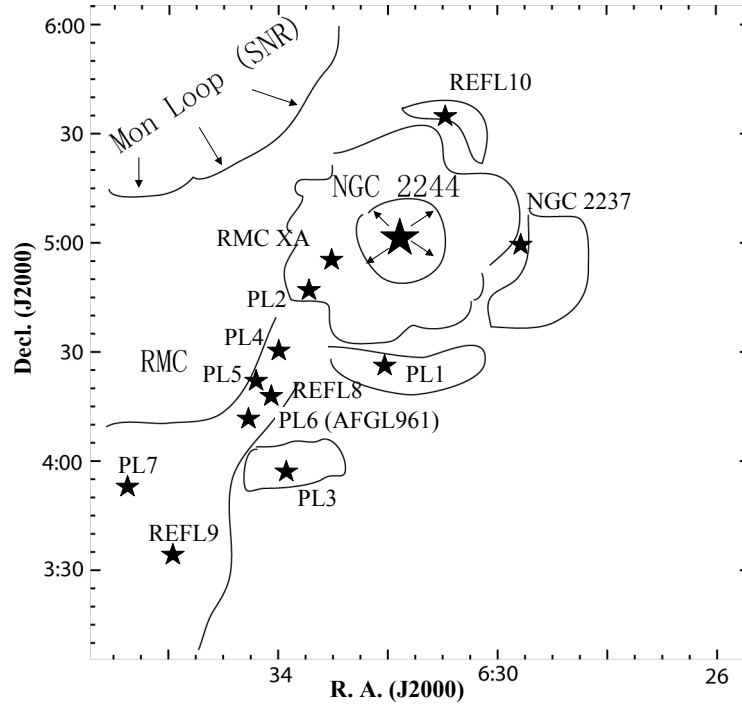


Figure 16(b)—Continued.